Neuron

Article

Physical and functional convergence of the autism risk genes *Scn2a* and *Ank2* in neocortical pyramidal cell dendrites

Highlights

- Ankyrin-B (*Ank2*) is expressed throughout neocortical pyramidal cell dendrites
- Ankyrin-B scaffolds the sodium channel $Na_V1.2$ (*Scn2a*) to dendritic membranes
- Haploinsufficiency in either *Ank2* or *Scn2a* impairs dendritic excitability
- Shared function suggests that dendritic dysfunction contributes to ASD etiology

Authors

Andrew D. Nelson, Amanda M. Catalfio, Julie P. Gupta, ..., Stephan J. Sanders, Kevin J. Bender, Paul M. Jenkins

Correspondence

kevin.bender@ucsf.edu (K.J.B.), pjenkins@umich.edu (P.M.J.)

In brief

Autism spectrum disorder (ASD) is associated with dysfunction in hundreds of genes. How dysfunction in ASD-associated genes converges on shared biological mechanisms remains an open question. Here, Nelson et al. show that one ASD-associated gene, *Ank2*, scaffolds another, *Scn2a*, in neocortical pyramidal cell dendrites, with shared effects on dendritic integration.

Nelson et al., 2024, Neuron *112*, 1133–1149
April 3, 2024
https://doi.org/10.1016/j.neuron.2024.01.003

CellPress

Neuron

CellPress

Article

Physical and functional convergence of the autism risk genes *Scn2a* and *Ank2* in neocortical pyramidal cell dendrites

Andrew D. Nelson,[1,2] Amanda M. Catalfio,[3] Julie P. Gupta,[3] Lia Min,[3] René N. Caballero-Florán,[3] Kendall P. Dean,[4] Carina C. Elvira,[4] Kimberly D. Derderian,[1,2] Henry Kyoung,[1,2] Atehsa Sahagun,[1,2] Stephan J. Sanders,[1,5] Kevin J. Bender,[1,2,*] and Paul M. Jenkins[3,6,7,*]

[1]Weill Institute for Neurosciences, University of California, San Francisco, San Francisco, CA, USA
[2]Department of Neurology, University of California, San Francisco, San Francisco, CA, USA
[3]Department of Pharmacology, University of Michigan Medical School, Ann Arbor, MI, USA
[4]Cellular and Molecular Biology Program, University of Michigan Medical School, Ann Arbor, MI, USA
[5]Department of Psychiatry, University of California, San Francisco, San Francisco, CA, USA
[6]Department of Psychiatry, University of Michigan Medical School, Ann Arbor, MI, USA
[7]Lead contact
*Correspondence: kevin.bender@ucsf.edu (K.J.B.), pjenkins@umich.edu (P.M.J.)
https://doi.org/10.1016/j.neuron.2024.01.003

SUMMARY

Dysfunction in sodium channels and their ankyrin scaffolding partners have both been implicated in neurodevelopmental disorders, including autism spectrum disorder (ASD). In particular, the genes *SCN2A*, which encodes the sodium channel $Na_V1.2$, and *ANK2*, which encodes ankyrin-B, have strong ASD association. Recent studies indicate that ASD-associated haploinsufficiency in *Scn2a* impairs dendritic excitability and synaptic function in neocortical pyramidal cells, but how $Na_V1.2$ is anchored within dendritic regions is unknown. Here, we show that ankyrin-B is essential for scaffolding $Na_V1.2$ to the dendritic membrane of mouse neocortical neurons and that haploinsufficiency of *Ank2* phenocopies intrinsic dendritic excitability and synaptic deficits observed in *Scn2a*$^{+/-}$ conditions. These results establish a direct, convergent link between two major ASD risk genes and reinforce an emerging framework suggesting that neocortical pyramidal cell dendritic dysfunction can contribute to neurodevelopmental disorder pathophysiology.

INTRODUCTION

A decade of gene discovery has identified hundreds of genes whose dysfunction is associated with autism spectrum disorder (ASD).[1–6] A key challenge remains to translate these findings into an understanding of pathophysiology at the cellular and circuit level. Loss of function in *SCN2A*, which encodes the neuronal sodium channel $Na_V1.2$, has the strongest evidence of ASD association based on exome sequencing.[6–9] Given this critical role in ASD etiology, alterations in cellular function due to *SCN2A* loss may illuminate common causes of dysfunction shared with other ASD-associated genes.

A novel role for $Na_V1.2$ was identified recently in neocortical pyramidal cells, a cell class whose dysfunction is implicated in ASD.[6,10] In contrast to well-characterized roles for sodium channels (Na_Vs) in axonal action potential (AP) electrogenesis and propagation, $Na_V1.2$ was found to be critical for dendritic excitability, with ASD-associated *Scn2a* haploinsufficiency impairing postsynaptic features of synaptic function and plasticity.[9] This dendritic $Na_V1.2$ localization is presumably controlled by ankyrins, which are a family of scaffolding proteins that link ion channels to the actin cytoskeleton.[11–13] Ankyrin-Na_V interactions have been studied extensively in the axon, where Na_Vs are anchored by ankyrin-G (*ANK3*),[14–17] but how Na_Vs are scaffolded to dendritic domains is unknown.

Insight may come from ASD gene discovery, which implicates dysfunction in another ankyrin family member, ankyrin-B (*ANK2*), in ASD.[6,8] Immunostaining for ankyrin-G and ankyrin-B in cultured neurons indicates that they occupy largely non-overlapping domains, with ankyrin-G enriched in the axon initial segment (AIS) and nodes of Ranvier, and ankyrin-B enriched in other regions, including dendrites.[18] Thus, ankyrin-B is well-positioned to scaffold dendritic $Na_V1.2$ channels. In this way, loss of function in either *SCN2A* or *ANK2* could impair dendritic excitability, either directly through reduced Na_V density or indirectly through reduced Na_V scaffolding.

Here, we show that the protein products of these two ASD risk genes, *SCN2A* and *ANK2*, interact in neocortical pyramidal cell dendrites to mutually regulate dendritic excitability. Using epitope-tagged $Na_V1.2$, we found that $Na_V1.2$ co-localizes with ankyrin-B in the dendrites of neocortical neurons. Removal of ankyrin-B eliminated $Na_V1.2$ dendritic localization. Furthermore,

dendritic ankyrin-B loss was not compensated for by other ankyrin family members, indicating that ankyrin-B has a unique scaffolding role in this neuronal compartment. *Ex vivo* electrophysiology revealed that *Ank2* haploinsufficiency results in intrinsic and synaptic dendritic deficits that closely phenocopy those observed in *Scn2a* heterozygous neurons. The direct convergence between *SCN2A* and *ANK2* shown here therefore further implicates deficits in dendritic excitability in ASD.

RESULTS

$Na_V1.2$ and ankyrin-B colocalize in neocortical neuron dendrites after the first postnatal week

To determine whether Na_Vs and ankyrins physically converge in dendrites, we first aimed to visualize their subcellular distribution patterns within a single cell. Although Na_Vs can be observed in the AIS and nodes of Ranvier using conventional immunostaining approaches, they are often too diffuse to detect reliably in other regions.[19] To visualize $Na_V1.2$ across development in all neuronal compartments, we first generated a cDNA encoding full-length $Na_V1.2$ with a 3xFLAG epitope tag on the carboxyl-terminal, in addition to IRES-mediated expression of freely diffusible GFP. Voltage-clamp recordings from HEK293 cells transfected with either wild-type (WT) $Na_V1.2$ or $Na_V1.2$-3xFLAG indicated that the introduction of this epitope tag did not alter channel biophysics (Figure S1A) or its ability to interact with β1 subunits (Figure S1B). For all experiments in cultured neurons, transfection efficiency was purposely held to low levels, often with only a single neuron transfected within a 1x1 mm field of view, to ensure that effects observed were due to cell-autonomous manipulations (Figure S2).

Immunostaining and electrophysiological measurements indicate that $Na_V1.2$ is enriched in the AIS of neocortical pyramidal cells in early development[20–23] (Figure 1A). Consistent with staining of native channels, $Na_V1.2$-3xFLAG was similarly restricted to the AIS at day *in vitro* 7 (DIV7) in cultured neocortical neurons, where it colocalized with ankyrin-G (Figure 1C). Later in development, $Na_V1.2$ is largely displaced from the AIS and instead increases in density throughout somatodendritic domains[9,24–27] (Figure 1A). Consistent with this shift in $Na_V1.2$ subcellular localization, $Na_V1.2$-3xFLAG was visualized at high levels throughout dendrites at DIV21 (Figure 1C). Dendritic $Na_V1.2$ was not co-localized with *ANK3* (Figure 1C), suggesting that another ankyrin may be important for Na_V scaffolding in dendritic regions. Based on genetic and co-expression data related to ASD[6,8,10] (Figure 1B), we hypothesized that this dendritic scaffold is ankyrin-B (*ANK2*).

To compare the subcellular localization patterns of ankyrin-B and $Na_V1.2$ across development, we transfected cultured neocortical neurons with $Na_V1.2$-3xFLAG-IRES-GFP and immunostained with antibodies against ankyrin-B at DIV7 and DIV21. At DIV7, ankyrin-B was localized to the distal axon (Figure 1D). At DIV21, however, ankyrin-B was enriched along dendritic shafts, colocalizing with $Na_V1.2$ (Figure 1D). $Na_V1.2$ expression remained in distal axons (Figures 1C and 1D), likely because neurons were not co-cultured with myelinating oligodendrocytes.[28–30] Importantly, there was no correlation between dendritic $Na_V1.2$-3xFLAG and plasmid expression levels, inferred from GFP fluorescence intensity, suggesting that $Na_V1.2$ expression is tightly regulated and that its dendritic localization is not an off-target effect of overexpression (Figure 1E). These data indicate that ankyrin-B is well-positioned to scaffold $Na_V1.2$ to neocortical pyramidal cell dendrites after early development.

Ankyrin-B localizes $Na_V1.2$ to the dendritic membrane of neocortical neurons

To determine whether ankyrin-B directly scaffolds $Na_V1.2$ to the dendritic membrane, we performed knockout-and-rescue experiments in cultured neocortical neurons generated from *Ank2*$^{fl/fl}$ mice, which contain *loxP* sites flanking exon 24 of the *Ank2* gene.[31] In WT conditions, $Na_V1.2$-3xFLAG was highly enriched in the dendritic membrane with endogenous ankyrin-B in DIV21 neurons (Figures 2A and S2A). Co-transfection of $Na_V1.2$-3xFLAG-IRES-GFP with Cre-2A-BFP (blue fluorescent protein) in *Ank2*$^{fl/fl}$ neurons resulted in the complete loss of ankyrin-B, with a corresponding loss of dendritic $Na_V1.2$ (Figure 2A). Simultaneous knockout of endogenous ankyrin-B via Cre-2A-BFP and rescue with the canonical WT ankyrin-B restored $Na_V1.2$ to dendritic membranes (Figure 2A). Similar reductions in dendritic $Na_V1.2$ localization were observed in *Ank2* heterozygous cultured neurons, as seen with full knockout, suggesting that even the loss of one functional *Ank2* allele is enough to decrease $Na_V1.2$ dendritic density to levels below detection threshold (Figures S4A–S4C).

Ankyrin-B is highly homologous with ankyrin-G, especially throughout the ankyrin repeat domain that contains the canonical Na_V binding site.[32] Therefore, we examined whether ankyrin-B requires this same sequence to localize $Na_V1.2$. We generated a double mutant (F131Q, F164Q) in the ankyrin repeats of ankyrin-B, which has been shown previously to reduce binding affinity between ankyrins and $Na_V1.2$ by >40-fold.[33] Knockout-and-rescue with the FF/QQ mutant failed to scaffold $Na_V1.2$ to the dendrites, demonstrating the importance of this site for the proper localization of $Na_V1.2$ to adult neocortical dendrites (Figure 2A). Importantly, $Na_V1.2$ clustered appropriately to the AIS in *Ank2* null and FF/QQ mutant neurons (Figure 2A). This suggests that the presence of $Na_V1.2$ in the dendrites is not an artifact of $Na_V1.2$-3xFLAG overexpression and requires ankyrin-B. In addition, the localization patterns of $Na_V1.2$-3xFLAG across these conditions are consistent with previous studies using two distinct methods to label endogenous $Na_V1.2$.[29,34]

Ankyrin-B is expressed as two splice variants in the brain that both contain the conserved Na_V-binding site[35]: a 220-kDa isoform and a giant 440-kDa isoform.[36] The 440-kDa ankyrin-B has been shown to be the primary isoform in the distal axon,[18,37,38] but which splice variant functions in the dendrites is less clear. Western blot analysis of mouse neocortical lysates from postnatal day (P)0 to P30 revealed parallel increases in $Na_V1.2$ and ankyrin-B expression throughout development (Figure 2B). Expression of the 220-kDa ankyrin-B, which has been shown to be more prominent later in development,[18,39] correlated more closely with $Na_V1.2$ expression than the 440-kDa ankyrin-B, suggesting that the 220-kDa ankyrin-B may be the main isoform that functions in the dendrites (Figure 2B). To evaluate

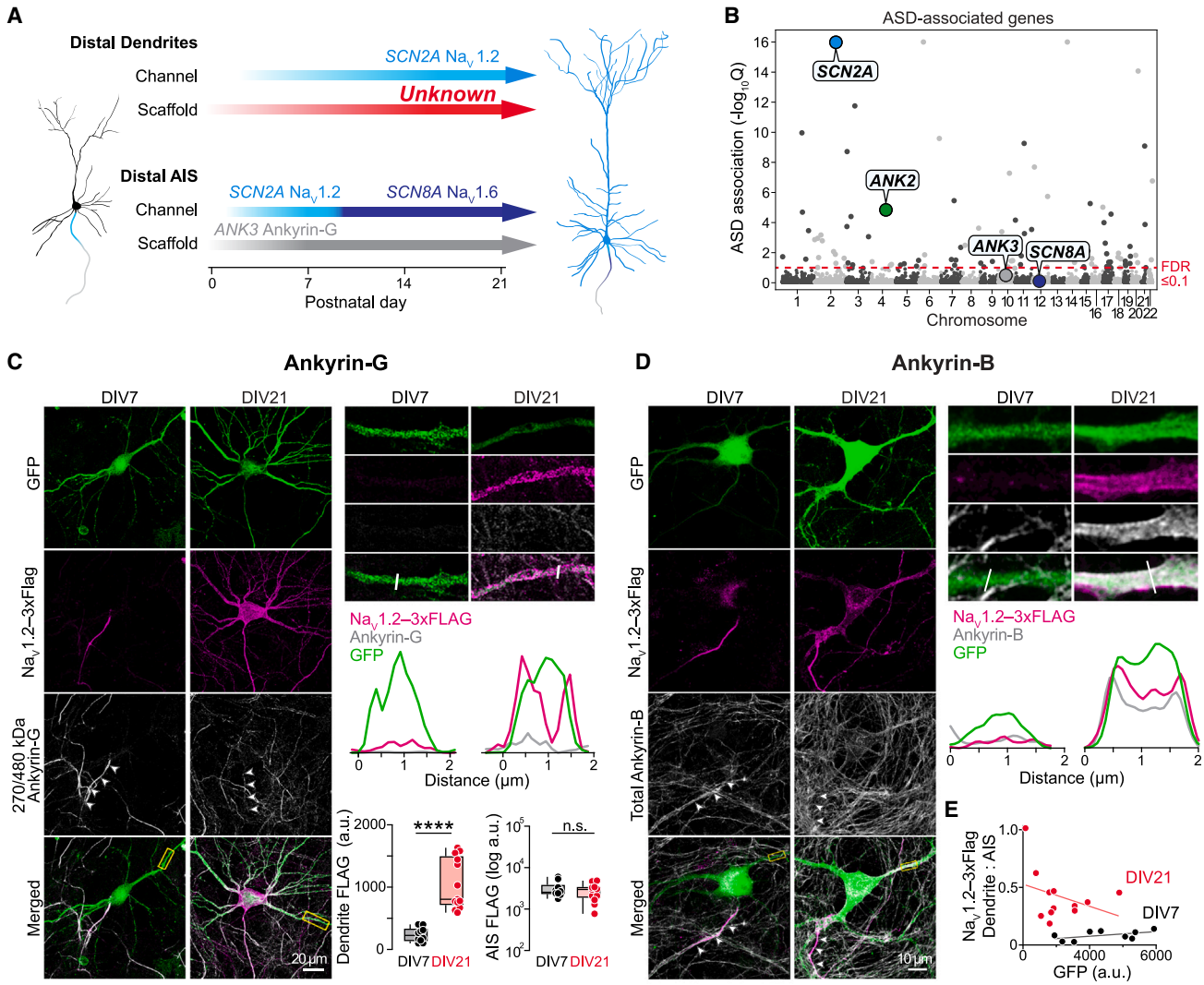

Figure 1. Ankyrin-B is colocalized with Na$_V$1.2 in the dendrites of mature pyramidal neurons

(A) Schematic of Na$_V$ channel distribution with ankyrins throughout neocortical pyramidal neuron development.

(B) Manhattan plot of ASD-associated genes identified by whole-exome sequencing. Red dotted line indicates false discovery rate threshold of $\leq$0.1.

(C) Left: confocal images of WT-cultured neocortical neurons transfected with Na$_V$1.2-3xFLAG-IRES-EGFP, fixed at DIV7 or DIV21. Cells were immunostained for ankyrin-G (white), FLAG (magenta), and GFP (green). Arrowheads denote AIS of transfected cell. Top right: zoomed image of dendrite labeled with yellow box. Middle right: plot profiles of dendritic Na$_V$1.2-3xFLAG, ankyrin-G, and GFP fluorescence intensity (a.u.) at DIV7 and DIV21. Dendritic region used to generate plot profile indicated by white line in above figure. Quantification of mean fluorescence intensity of Na$_V$1.2-3xFLAG in dendrites or AIS at DIV7 vs. DIV21. Circles represent individual neurons. Dendrites:(DIV7: 237.4 ± 36.0, n = 10 cells; DIV21: 1,046 ± 111.8, n = 13 cells) ****p < 0.0001. AIS:(DIV7: 3,134 ± 444.5, n = 10 cells; DIV21: 2,798 ± 334.7, n = 13 cells) p = 0.83. No significant differences.

(D) Left: confocal images of Na$_V$1.2-3xFLAG-IRES-EGFP-transfected cells, as in (C), but immunostained for ankyrin-B instead of ankyrin-G.

(E) Linear regression of mean Na$_V$1.2-3xFLAG dendrite:AIS fluorescent signal vs. GFP at DIV7 and DIV21.

localization patterns of the 220- vs. the 440-kDa ankyrin-B, we cloned full-length 220-kDa ankyrin-B-GFP and 440-kDa ankyrin-B-GFP. Constructs were expressed in cultured neocortical neurons and immunostained with antibodies against GFP and ankyrin-G. As previously shown, the 440-kDa ankyrin localized almost exclusively to the distal axon (Figures 2C and 2D). By contrast, the 220-kDa isoform localized throughout the entire dendritic arbor, the soma, and the axon (Figures 2C–2E). Overall, these data indicate that the 220-kDa ankyrin-B is the predominant ankyrin that targets Na$_V$1.2 channels to pyramidal cell dendrites.

Ankyrin-B directly interacts with Na$_V$1.2 in mouse brain

We next evaluated the molecular basis underlying the interaction between ankyrin-B and dendritic Na$_V$1.2. Due to their large size, it is difficult to study direct protein-protein interactions between full-length ankyrins and ion channels.[12,40] Therefore, we evaluated binding between ankyrin-B-GFP and an epitope-tagged

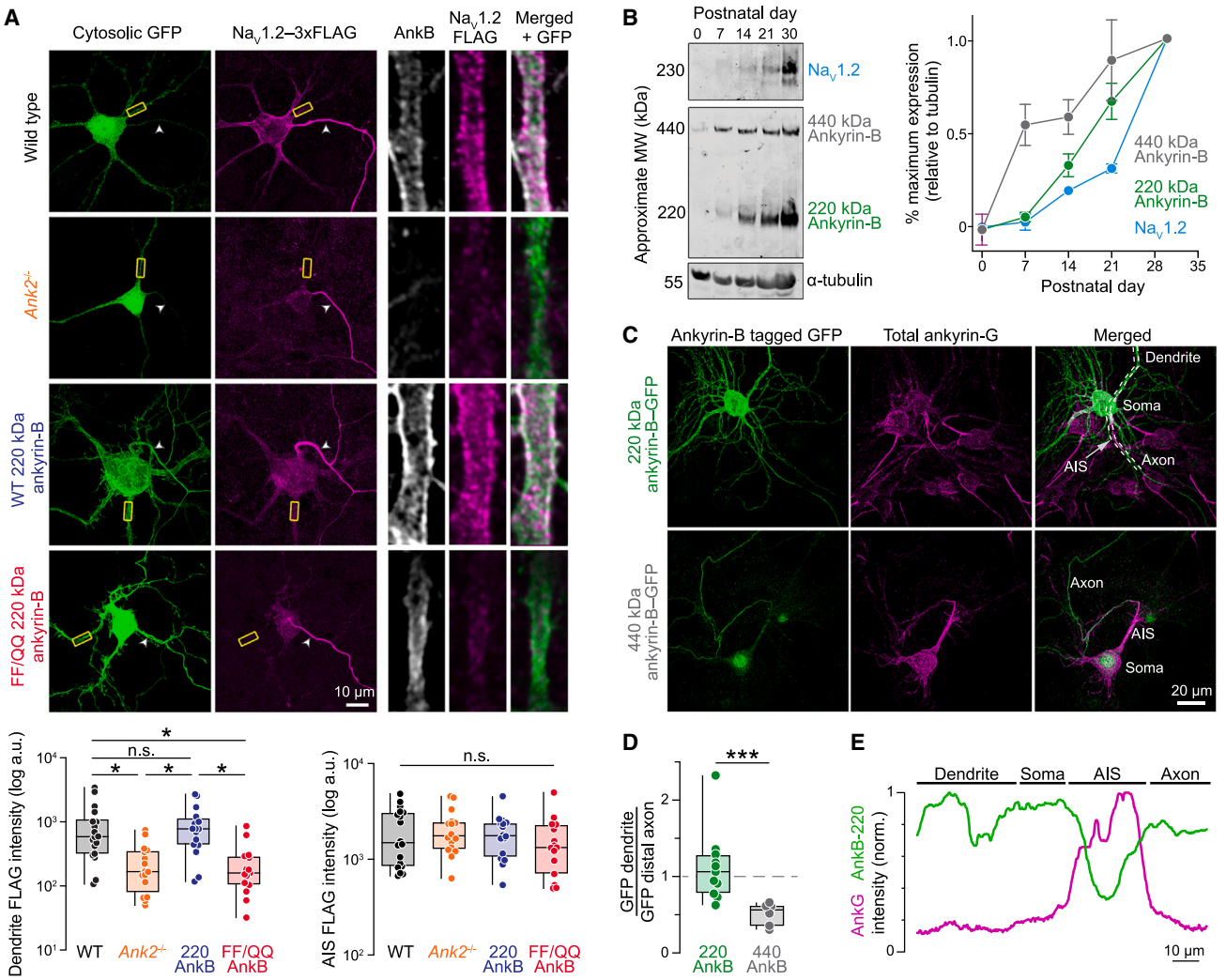

Figure 2. 220 kDa ankyrin-B scaffolds Na$_V$1.2 to the dendritic membrane

(A) Top left: confocal images of DIV21 *Ank2*$^{flox/flox}$-cultured neocortical neurons co-transfected with Na$_V$1.2-3xFLAG-IRES-EGFP and TagBFP (WT) or Cre-2A-BFP (*Ank2* null), or rescued with WT or FF/QQ mutant 220 kDa ankyrin-B. Cells were immunostained for ankyrin-B (white), FLAG (magenta), and GFP (green). Top right: zoomed images of dendrite labeled with yellow box. Bottom left: Quantification of mean fluorescence intensity of Na$_V$1.2-3xFLAG in dendrites. Circles represent individual neurons. Dendrites:(WT: 933.0 ± 218.8, n = 18 cells; *Ank2*$^{-/-}$: 246.0 ± 51.16, n = 16 cells; *Ank2*$^{-/-}$ + WT 220 kDa AnkB: 945.1 ± 191.8, n = 16 cells; *Ank2*$^{-/-}$ + FF/QQ 220 kDa AnkB: 237.3 ± 57.9, n = 15 cells). WT vs. *Ank2*$^{-/-}$ *p = 0.016, *Ank2*$^{-/-}$ vs. 220 AnkB *p = 0.016, WT vs. FF/QQ AnkB *p = 0.016, 220 AnkB vs. FF/QQ AnkB *p = 0.016. Bottom right: quantification of mean fluorescence intensity of Na$_V$1.2-3xFLAG in the AIS. AIS: (WT: 2,046 ± 309.2, n = 18 cells; *Ank2*$^{-/-}$: 2,123 ± 282.9, n = 16 cells; *Ank2*$^{-/-}$ + WT 220 kDa AnkB: 1,900 ± 241.3, n = 16 cells; *Ank2*$^{-/-}$ + FF/QQ 220 kDa AnkB: 1,627 ± 981.3, n = 15 cells). No significant differences. Arrowhead marks the AIS.

(B) Left: western blot of WT mouse neocortical lysates at P0, P7, P14, P21, and P30. Blots were probed with antibodies to endogenous total ankyrin-B (labeling both 440-kDa [gray] and 220-kDa [green] ankyrin-B isoforms), Na$_V$1.2 (cyan), and α-tubulin. Right: western blot data, normalized to expression at P30. N = 3 mice per age. Data shown as mean ± SEM.

(C) Confocal images of WT-cultured neurons transfected with 220-kDa AnkB-GFP or 440-kDa AnkB-GFP, fixed at DIV21. Neurons were immunostained for endogenous ankyrin-G (magenta) and GFP (green).

(D) Mean fluorescence intensity (a.u.) ratio of dendritic and distal axon GFP from 220-kDa ankyrin-B (green) vs. 440-kDa ankyrin-B (gray) in (C). (220-kDa AnkB: 1.12 ± 0.14, n = 11 cells; 440-kDa AnkB: 0.51 ± 0.06, n = 6 cells). ***p = 0.0003.

(E) Plot profiles of mean fluorescence intensity (a.u.) of transfected 220-kDa ankyrin-B-GFP vs. endogenous total ankyrin-G across different neuronal domains in (C). White dashes indicate regions measured.

fragment of Na$_V$1.2 that contains a highly conserved core nine amino acid motif necessary for ankyrin binding (Na$_V$1.2 II-III loop-hemagglutinin [HA])[12] (Figure 3A). We co-transfected these constructs in HEK293 cells and performed a proximity ligation assay (PLA), finding that ankyrin-B and the Na$_V$1.2 II-III loop associate within 10 nm of each other (Figure 3B). To assess direct binding between ankyrin-B and Na$_V$1.2, we then transfected HEK293 cells with a mutant Na$_V$1.2 II-III loop (termed

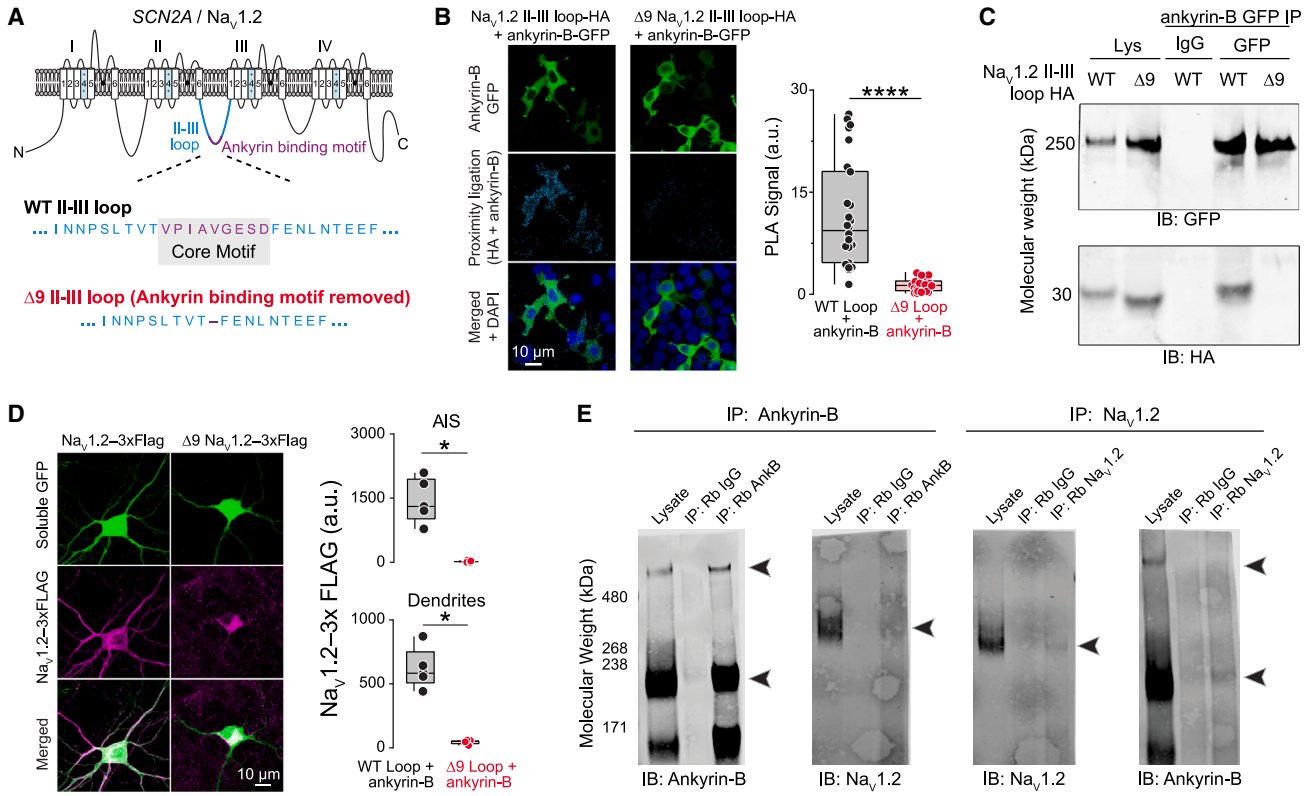

Figure 3. Ankyrin-B directly interacts with $Na_V1.2$ in the adult mouse brain

(A) $Na_V1.2$ schematic highlighting the ankyrin-binding motif (purple) located within the intracellular loop between domains II and III (cyan). Core nine amino acids (Δ9 motif) within the II-III loop are essential for ankyrin binding.

(B) Left: representative images of proximity ligation assay (PLA) signal (cyan) between anti-HA and anti-ankyrin-B antibodies from HEK293 cells transfected with 220-kDa ankyrin-B-GFP (green) and HA-tagged $Na_V1.2$ II-III loop (left), or the HA-tagged Δ9 mutant loop (right). Right: quantification of PLA signal (a.u.) between ankyrin-B and WT $Na_V1.2$ II-III loop vs. ankyrin-B and Δ9 $Na_V1.2$ II-III loop. (WT: 11.6 ± 1.5, n = 26 cells; Δ9: 1.4 ± 0.2, n = 24 cells). ****p < 0.0001.

(C) Co-immunoprecipitation of ankyrin-B-GFP with WT $Na_V1.2$ II-III loop or Δ9 $Na_V1.2$ II-III loop. Western blots were probed with antibodies against anti-GFP (to label ankyrin-B-GFP) and anti-HA (to label $Na_V1.2$ II-III loop-HA). Non-immune IgG used as a negative control.

(D) Left: confocal images of cultured neocortical neurons transfected with WT $Na_V1.2$-3xFLAG-IRES-EGFP or Δ9 $Na_V1.2$-3xFLAG-IRES-EGFP. Cells were immunostained with anti-GFP (green) and anti-FLAG (magenta) antibodies. Right: mean fluorescence intensity (a.u.) of $Na_V1.2$-3xFLAG in the AIS (top) and dendrites (bottom). AIS: (WT: 1,445 ± 233.5, n = 5 cells; Δ9: 17.06 ± 15.2, n = 4 cells). *p = 0.016. Dendrites: (WT: 620 ± 71.0, n = 5 cells; Δ9: 46.1 ± 9.7, n = 4 cells). *p = 0.016.

(E) Left: IP of endogenous ankyrin-B and western blot of IP lysates probed with antibodies to ankyrin-B or endogenous $Na_V1.2$ from P60 to P75 mice. Right: IP of endogenous $Na_V1.2$ and western blot of IP lysates probed with antibodies to $Na_V1.2$ or ankyrin-B from P60 to P75 mice. Black arrows highlight bands of ankyrin-B or $Na_V1.2$. Non-immune IgG used as a negative control. Note: 440-kDa ankyrin-B band consistently runs anomalously high, as reported previously.[14]

Δ9-mutant $Na_V1.2$) from which we excised the core 9 amino acid ankyrin-binding motif. Expression of the Δ9-mutant $Na_V1.2$ completely abolished PLA signal, highlighting this motif's importance for ankyrin-B-$Na_V1.2$ binding (Figure 3B). Of note, deletion of the Δ9 sequence in the $Na_V1.2$-3xFLAG construct did not affect channel biophysical properties (Figure S1C). We further validated their interaction by immunoprecipitating ankyrin-B-GFP and $Na_V1.2$ II-III loop from HEK293 cells (Figures 3C and S5). Again, we failed to detect any Δ9-mutant $Na_V1.2$ following immunoprecipitation (IP) of ankyrin-B (Figures 3C and S5).

We next tested whether ankyrin-B localized full-length $Na_V1.2$ in pyramidal cell dendrites if $Na_V1.2$ lacked the ankyrin-binding motif. Cultured neurons were transfected with plasmids encoding either WT $Na_V1.2$-3xFLAG-IRES-GFP or Δ9 $Na_V1.2$-3xFLAG-IRES-GFP. At DIV21, WT $Na_V1.2$-3xFLAG properly localized to the dendrites and the AIS; however, the Δ9-mutant $Na_V1.2$-3xFLAG-IRES-GFP, which is unable to interact with ankyrin-B, failed to localize to the dendrites (Figure 3D). Because excising the nine amino acid motif prevents all ankyrins from binding, $Na_V1.2$-3xFLAG clustering at the AIS was also lost (Figure 3D). These Δ9-mutant $Na_V1.2$ data are consistent with those obtained with the FF/QQ mutant ankyrin-B, further confirming that dendritic localization of $Na_V1.2$-3xFLAG is not an artifact of overexpression.

The above experiments demonstrate that ankyrin-B is in complex with $Na_V1.2$ in pyramidal neuron dendrites when each protein is overexpressed in cultured neocortical neurons. To determine whether this interaction occurs with endogenous ankyrin-B and $Na_V1.2$ in native adult neocortex, we immunoprecipitated ankyrin-B using antibodies that detect both the 220- and

440-kDa isoforms. Western blot and immunoblotting with antibodies against $Na_V1.2$ revealed that ankyrin-B is in complex with $Na_V1.2$ in the adult neocortex (Figures 3E and S7). Because ankyrin-B is expressed in almost every cell type within the neocortex,[39] we wanted to confirm their interaction in pyramidal cell dendrites, where $Na_V1.2$ predominantly resides, by immunoprecipitating $Na_V1.2$ from the adult brain. IP of $Na_V1.2$ resulted in co-immunoprecipitation (coIP) of the dendritic 220-kDa ankyrin-B (Figure 2C), but not the 440-kDa isoform, which is predominantly axonal (Figure 3E). These data provide further evidence that the 220-kDa ankyrin-B is the primary isoform that interacts with $Na_V1.2$ in the adult mouse brain and demonstrates that endogenous $Na_V1.2$ is associated in complex with ankyrin-B in the adult neocortex.

Ank2 haploinsufficiency impairs dendritic, but not somatic, excitability

$Na_V1.2$ channels are expressed on both somatic and dendritic membranes in neocortical pyramidal neurons. The data above indicate that ankyrin-B is important for dendritic Na_V scaffolding; however, previous reports have demonstrated that both ankyrin-B and ankyrin-G are present on the soma of mature pyramidal neurons.[14,41,42] As such, *Ank2* haploinsufficiency is expected to impair measures of dendritic excitability, but whether somatic excitability is also affected may depend instead on how channels interact with ankyrin-G at the soma. Previously, we used the peak velocity of the rising phase of the AP (peak dV/dt) and AP-evoked dendritic calcium imaging as functional proxies for $Na_V1.2$ membrane density in the somatic and dendritic compartments, respectively.[9,26] Thus, these approaches may help reveal functional changes in $Na_V1.2$ density in somatic and dendritic compartments in cases of *Ank2* loss.

In prior studies on *Scn2a*, we found that haploinsufficiency, either throughout life or induced after P16, resulted in identical deficits in dendritic excitability and excitatory synaptic function.[9] Furthermore, we leveraged genetic approaches in ~P30 *Scn2a*$^{+/-}$ mice to restore *Scn2a* expression and rescue downstream excitability deficits to WT levels.[43] This suggests that *Scn2a* has a lifelong role in regulating dendritic excitability and that our studies here should focus on this developmental period to assess potential convergent function between *Scn2a* and *Ank2*. Therefore, we examined AP waveform properties from layer 5 (L5) thick-tufted neurons in acute slices of P43–P75 *Ank2*$^{+/fl}$::CaMKIIα-Cre mice, which express Cre in all neocortical pyramidal neurons after ~P16[9,44] (Figures 4A–4E and S6). Western blots of neocortical lysates generated from adult *Ank2*$^{+/fl}$::CaMKIIα-Cre mice revealed a reduction in the 440- and 220-kDa isoforms of ankyrin-B without any change in $Na_V1.2$ or ankyrin-G expression (Figure S7). Although interleaved experiments in *Scn2a*$^{+/-}$ cells revealed expected reductions in peak somatic dV/dt, *Ank2*$^{+/fl}$ cells were no different than WT (Figures 4D and 4E). In addition, we observed no difference in the AP firing per current injection (F/I curve) of *Ank2*$^{+/fl}$ neurons compared with WT and *Scn2a*$^{+/-}$ neurons, or in measures of AIS excitability (threshold and AIS-associated peak dV/dt) (Figures 4B–4E).

These empirical data suggest that loss of *Ank2* does not affect somatic or axonal excitability, contrasting with previous results in *Scn2a*$^{+/-}$ neurons and with compartmental models where *Ank2* haploinsufficiency induces a reduction in $Na_V1.2$ density throughout the somatodendritic domain (Figure 4F). Instead, models indicate that peak dV/dt depends exclusively on somatic Na_V density and is insensitive to changes in dendritic channel density (Figure 4G), therefore suggesting that $Na_V1.2$ densities are at WT levels in *Ank2*$^{+/-}$ cells in the soma. This motivated us to examine somatic $Na_V1.2$-3xFLAG labeling in cultured *Ank2*$^{-/-}$ neurons. Consistent with measures of excitability, $Na_V1.2$-3xFLAG was localized to the soma in these cells at WT levels (Figure 4H). Thus, ankyrin-G may either be the primary ankyrin that localizes $Na_V1.2$ to the soma or may be able to compensate for somatic ankyrin-B loss in both heterozygous or homozygous knockout conditions.

Although somatic recordings suggest that somatic Na_V density is not affected by *Ank2* haploinsufficiency, they cannot inform on changes in dendritic excitability, which modeling suggests would still be impaired in *Ank2*$^{+/-}$ conditions (Figure S6B). To evaluate the effects of ankyrin-B loss on dendritic Na_V channel density and excitability, we first examined dendritic Na_V function directly with AP-evoked Na^+ imaging, using the sodium indicator ING-2.[45–47] In WT neurons, trains of 40 APs at 100 Hz evoked detectable sodium transients within the first 125 μm of the apical dendrite (Figure 5A). At 25 μm from the soma, Na^+ transient amplitudes were comparable in WT and *Ank2*$^{+/-}$ neurons. In *Scn2a*$^{+/-}$ neurons, Na^+ influx was reduced by 50%, consistent with haploinsufficiency of Na_V density. Farther from the soma, however, transients in *Ank2*$^{+/-}$ neurons became significantly smaller and exhibited a 40% reduction in Na^+ influx compared with WTs (Figures 5A and 5B). This stark change in Na^+ influx between 25 and 50 μm from the soma corresponds well to the distribution of endogenous ankyrin-G, which can extend into the first tens of microns of a dendrite in cultured neurons (Figure 2C).[41]

Ankyrin-B has been reported to interact with Ca_V2 and Ca_V3 channels.[48–50] Thus, it is possible that results observed above may reflect a loss of Ca_V-mediated electrogenesis that, in turn, affects Na_V activity. To control for this possibility, we repeated experiments in the presence of Ca_V2 and Ca_V3 antagonists conotoxin-MVIIC and TTA-P2. We further included nifedipine to antagonize Ca_V1 channels, as Ca_V1 channels interact with ankyrin-B in cardiomyocytes and are expressed in neocortical pyramidal cell dendrites.[51,52] Data obtained with Ca_V antagonists were identical to those obtained without (Figures 5D–5F). Hence, these data are most consistent with a model where ankyrin-G is capable of scaffolding Na_Vs in the soma and proximal dendrite in *Ank2* haploinsufficient conditions, but that ankyrin-B is solely responsible for Na_V scaffolding in more distal dendritic domains.

Due to the low sensitivity inherent to Na^+ imaging, dendritic Na^+ influx could be imaged only within 150 μm of the soma. To understand how *Ank2* haploinsufficiency affects excitability in more distal dendritic compartments, we took advantage of the fact that bursts of backpropagating APs (bAPs) reliably engage Ca_Vs throughout the dendritic arbor.[9,53–56] Consistent with previous observations, bursts of APs (a set of 5 AP doublets at 100 Hz) evoked robust calcium transients throughout the apical dendrite of WT neurons (Figure 6B). By contrast, Ca^{2+} transients

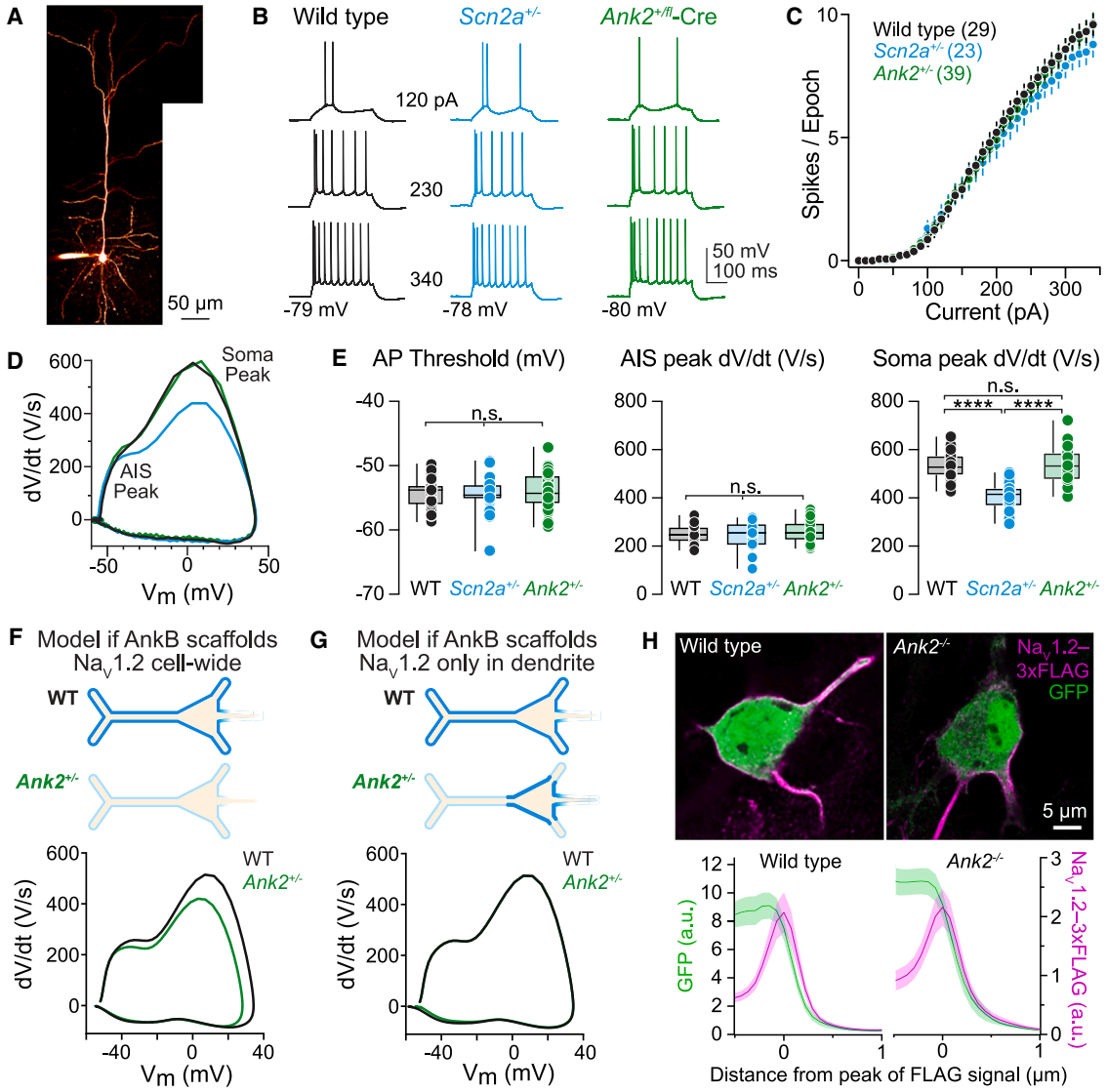

Figure 4. *Ank2* haploinsufficiency has no effect on axonal or somatic excitability

(A) Two-photon maximum intensity z stack of a layer 5 thick-tufted pyramidal neuron in mPFC, filled with Alexa 594 via whole-cell pipette.

(B) APs generated by current injection (0–340 pA, 10 pA intervals, 300 ms) in WT, *Scn2a*$^{+/-}$, and *Ank2*$^{+/fl}$-Cre in P43–P75 L5 neurons.

(C) APs per 300-ms epoch vs. amplitude of current injection as in (B). Firing-rate slope between 0 and 340 pA: (WT: 0.033 ± 0.002 Hz/pA, n = 29 cells, N = 14 mice; *Scn2a*$^{+/-}$: 0.03 ± 0.002 Hz/pA, n = 23 cells, N = 8 mice; *Ank2*$^{+/fl}$-Cre: 0.033 ± 0.001, n = 39 cells, N = 16 mice). No significant differences.

(D) Phase-plane plots (dV/dt vs. voltage) of somatic APs from WT (black), *Scn2a*$^{+/-}$ (cyan), and *Ank2*$^{+/fl}$-Cre (green) neurons. Different phases of the AP correspond to AP initiation in the AIS (first peak) and soma (second peak).

(E) Left: quantification of AP threshold (mV) from the first AP evoked by near-rheobase current in P43–P75 WT, *Scn2a*$^{+/-}$, and *Ank2*$^{+/fl}$-Cre L5 neurons. Circles represent single cells (WT: −54.4 ± 0.4 mV, n = 27 cells; *Scn2a*$^{+/-}$: −54.5 ± 0.4 mV, n = 23 cells; *Ank2*$^{+/fl}$-Cre: −53.9 ± 0.5 mV, n = 39 cells). No significant differences. Middle: AIS AP peak dV/dt (V/s). (WT: 248.7 ± 7.1 V/s, n = 27 cells; *Scn2a*$^{+/-}$: 242.2 ± 12.3 V/s, n = 23 cells; *Ank2*$^{+/fl}$-Cre: 257.6 ± 6.8 V/s, n = 39 cells). No significant difference. Right: somatic AP peak dV/dt (V/s) (WT: 537.8 ± 11.3 V/s, n = 27 cells; *Scn2a*$^{+/-}$: 406.4 ± 11.3 V/s, n = 27 cells, *Ank2*$^{+/fl}$-Cre: 535.1 ± 10.8 V/s, n = 40 cells). WT vs. *Scn2a*$^{+/-}$ ****p < 0.0001, *Scn2a*$^{+/-}$ vs. *Ank2*$^{+/fl}$-Cre ****p < 0.0001, WT vs. *Ank2*$^{+/fl}$-Cre p = 0.86.

(F) Compartmental modeling of the effects of $Na_V1.2$ loss from both somatic and dendritic domains on AP waveform. Top: schematic of $Na_V1.2$ distribution across soma and dendrites in WT neurons compared with loss of $Na_V1.2$ in all compartments in *Ank2*$^{+/fl}$-Cre neurons. Bottom: phase-plane plots from computational model of AP somatic peak dV/dt changes with WT and heterozygous $Na_V1.2$ membrane density. No other channels or model parameters were altered except for $Na_V1.2$.

(G) Modeling as in (F), but now restricting $Na_V1.2$ loss to dendrites alone. Note agreement of model with empirical data from *Ank2*$^{+/fl}$-Cre neurons in (E).

(H) Top: confocal images of DIV21 WT and *Ank2*-null-cultured neocortical neurons transfected with $Na_V1.2$-3xFLAG-IRES-EGFP and immunostained for FLAG (magenta) and GFP (green). Images are single optical sections through the soma. Complete z-projection images are shown in Figure S3. Bottom: somatic $Na_V1.2$-3xFLAG and GFP mean fluorescence intensity (a.u.) in WT (left) and *Ank2*-null (right) neurons. Lines are means with SEM shadows of 1-µm wide intensity profiles drawn orthogonal to the somatic membrane (2 lines per cell, 12 cells per condition).

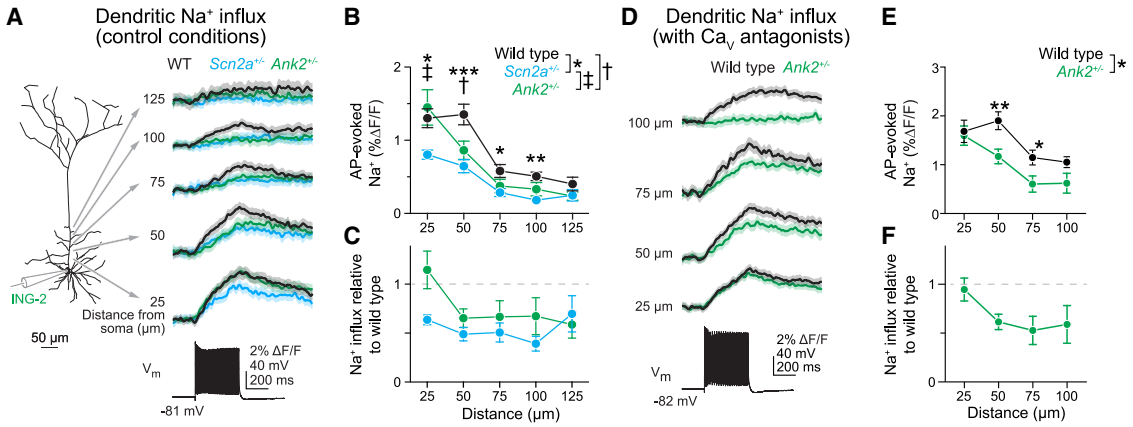

Figure 5. Reduced AP-evoked Na^+ apical dendrites of *Ank2* haploinsufficient neurons

(A) Two-photon Na^+ imaging throughout the apical dendrite of a L5 thick-tufted neuron filled with ING-2 (500 μM) via the recording pipette. Na^+ transients evoked by trains of APs (stimulus: 40× 100 Hz, 2 nA for 2 ms) every 25 μm from the soma in WT (black), *Scn2a*$^{+/-}$ (cyan) and *Ank2*$^{+/fl}$:: CaMKIIα-Cre (green) P46–P76 mice. Representative traces shown as mean ± SEM.

(B) AP-evoked Na^+ transient amplitude vs. distance from soma. 25 μm: (WT: 0.013 ± 0.001, n = 11 cells, N = 5 mice; *Scn2a*$^{+/-}$: 0.008 ± 0.0006, n = 12 cells, N = 3 mice; *Ank2*$^{+/fl}$-Cre: 0.015 ± 0.002, n = 8 cells, N = 3 mice) WT vs. *Scn2a*$^{+/-}$ *p = 0.03, WT vs. *Ank2*$^{+/fl}$-Cre p = 0.49, *Scn2a*$^{+/-}$ vs. *Ank2*$^{+/fl}$-Cre ‡p = 0.01. 50 μm: (WT: 0.014 ± 0.001, n = 11 cells; *Scn2a*$^{+/-}$: 0.007 ± 0.001, n = 12 cells; *Ank2*$^{+/fl}$-Cre: 0.009 ± 0.001, n = 8 cells) WT vs. *Scn2a*$^{+/-}$ ***p = 0.0004, WT vs. *Ank2*$^{+/fl}$-Cre †p = 0.02, *Scn2a*$^{+/-}$ vs. *Ank2*$^{+/fl}$-Cre p = 0.23. 75 μm: (WT: 0.006 ± 0.001, n = 8 cells; *Scn2a*$^{+/-}$: 0.003 ± 0.001, n = 9 cells; *Ank2*$^{+/fl}$-Cre: 0.004 ± 0.001, n = 8 cells) WT vs. *Scn2a*$^{+/-}$ *p = 0.04, WT vs. *Ank2*$^{+/fl}$-Cre p = 0.17, *Scn2a*$^{+/-}$ vs. *Ank2*$^{+/fl}$-Cre p = 0.42. 100 μm: (WT: 0.005 ± 0.001, n = 11 cells; *Scn2a*$^{+/-}$: 0.0018 ± 0.0004, n = 11 cells; *Ank2*$^{+/fl}$-Cre: 0.003 ± 0.001, n = 7 cells) WT vs. Scn2a$^{+/-}$ **p = 0.001, WT vs. *Ank2*$^{+/fl}$-Cre p = 0.11, *Scn2a*$^{+/-}$ vs. *Ank2*$^{+/fl}$-Cre p = 0.11. 125 μm: (WT: 0.004 ± 0.001, n = 8 cells; *Scn2a*$^{+/-}$: 0.002 ± 0.001, n = 7 cells; *Ank2*$^{+/fl}$-Cre: 0.002 ± 0.001, n = 6 cells) WT vs. *Scn2a*$^{+/-}$ p = 0.4, WT vs. *Ank2*$^{+/fl}$-Cre p = 0.4, *Scn2a*$^{+/-}$ vs. *Ank2*$^{+/fl}$-Cre p = 0.9. Data shown as mean ± SEM.

(C) Na^+ influx normalized to WT average at each distance.

(D) Two-photon Na^+ imaging as in (A) and (B), but in the presence of the Ca_V antagonists TTA-P2 (2 μM), nifedipine (10 μM), and conotoxin MVIIC (1 μM). Data from P63 to P81 mice.

(E) AP-evoked Na^+ transient amplitude in the presence of the Ca_V blockers vs. distance from soma. 25 μm: (WT: 0.017 ± 0.01, n = 8 cells, N = 3 mice; *Ank2*$^{+/fl}$-Cre: 0.016 ± 0.02, n = 8 cells, N = 3 mice) p = 0.64. 50 μm: (WT: 0.019 ± 0.002, n = 8 cells; *Ank2*$^{+/fl}$-Cre: 0.012 ± 0.002, n = 8 cells) **p = 0.007. 75 μm: (WT: 0.01 ± 0.007, n = 8 cells; *Ank2*$^{+/fl}$-Cre: 0.006 ± 0.002, n = 8 cells) *p = 0.038. 100 μm: (WT: 0.012 ± 0.001, n = 8 cells; *Ank2*$^{+/fl}$-Cre: 0.006 ± 0.002, n = 6 cells) p = 0.06. Data shown as mean ± SEM.

(F) Na^+ influx with Ca_V antagonists, normalized as in (C).

were reduced markedly in the *Ank2*$^{+/-}$ neurons, mirroring observations made in *Scn2a*$^{+/-}$ neurons[9] (Figure 6B). Of note, dendritic arborization was unaltered in adult L5 *Ank2*$^{+/-}$ neurons, with no difference in branch number or length compared with WT neurons (Figure S8A). Taken together, these data demonstrate that *Ank2* and *Scn2a* converge to regulate dendritic, but not somatic, intrinsic excitability.

Ank2 heterozygous mice exhibit impaired excitatory synaptic function

In *Scn2a*$^{+/-}$ cells, impaired dendritic excitability weakens postsynaptic aspects of excitatory synaptic transmission by reducing the relative number of functionally mature, AMPA-receptor-containing synapses.[9] We hypothesized that similar impairments may result from *Ank2* loss. To test this, we evaluated pre- and postsynaptic components of synaptic function in *Ank2*$^{+/fl}$ mice injected with a Cre-expression adeno-associated virus (AAV-EF1α-Cre-mCherry, injections at P30, experiments at P52–P60) (Figure 6A). Whole-cell voltage-clamp recordings of miniature excitatory and inhibitory postsynaptic currents (mEPSC, mIPSC) revealed a 50% reduction in mEPSC frequency, with no change in mEPSC amplitude (Figure 6C). mIPSC frequency and amplitude were unaffected (Figure S9).

These data are consistent with a reduction in the number of functionally mature, AMPA-receptor-containing excitatory synapses that were observed in *Scn2a*$^{+/-}$ conditions; however, reductions in release probability can also contribute to such observations. We therefore examined paired-pulse ratio (PPR) of evoked, AMPA-receptor-mediated currents, as this ratio is often inversely correlated with release probability. We observed a small decrease, rather than an increase, in PPR (Figure 6D). Taken together, these data support a model where a large fraction of synapses lack AMPA receptors and are silent in mEPSC recordings, and that release probability may be higher, at least at synapses that have AMPA receptors. To further test for the presence of silent synapses, we performed three additional experiments. First, we measured the AMPA:NMDA ratio, finding that it was reduced in *Ank2*$^{+/-}$-Cre neurons (Figure 6E). This is consistent with prior observations in *Scn2a*$^{+/-}$ mice and with an increased number of silent synapses.[9] Second, we tested for the presence of NR2B-containing NMDA receptors more commonly localized to immature, silent synapses.[57] We found that evoked NMDA-receptor-mediated EPSCs were more sensitive to the NR2B-selective antagonist Ro 25-6981 (1 μM) in both *Ank2*$^{+/-}$ and *Scn2a*$^{+/-}$ conditions compared with WT controls (Figure 6F). Lastly, we examined spine morphology in *Ank2*$^{+/-}$

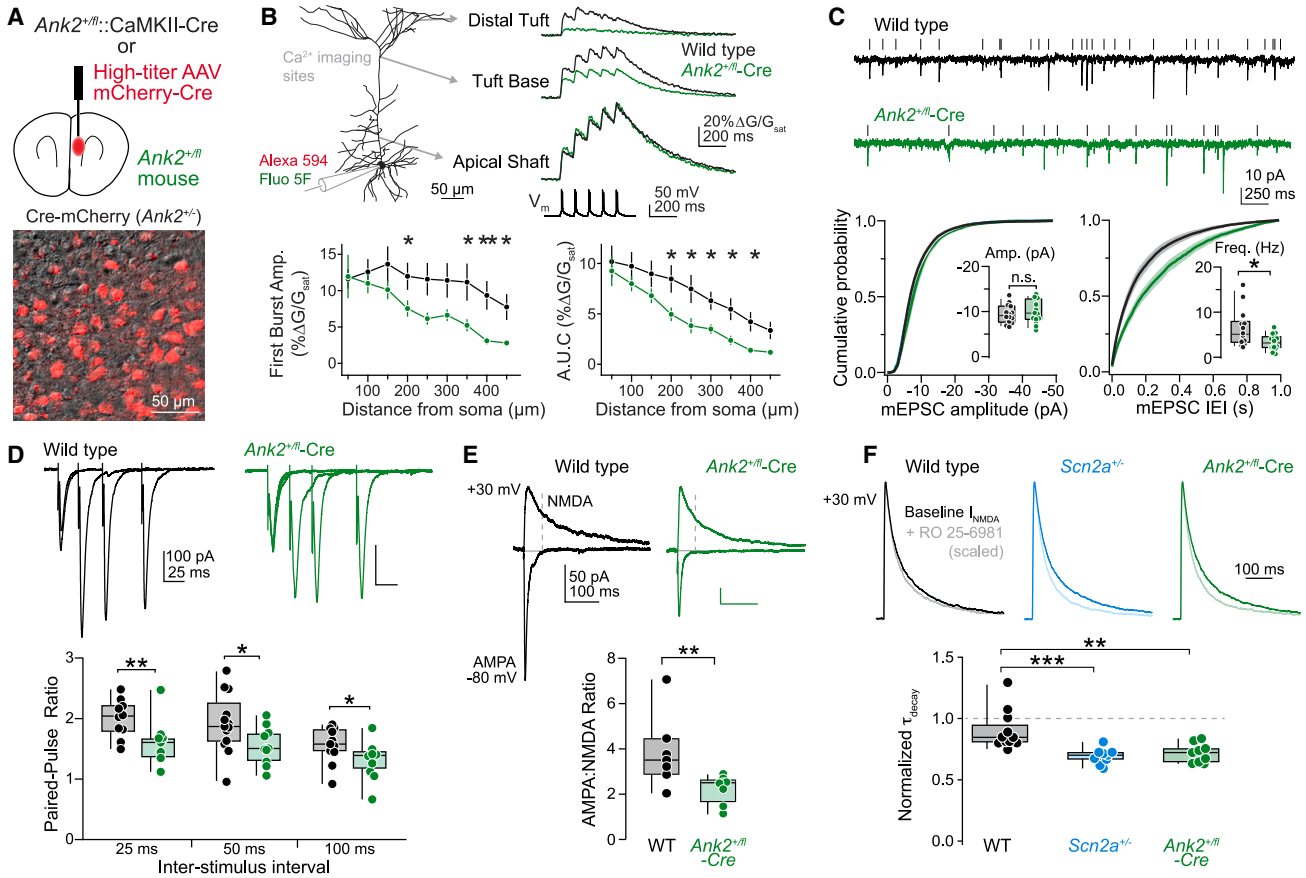

Figure 6. *Ank2* haploinsufficiency impairs dendritic backpropagation of APs and excitatory synapse function

(A) *Ank2*$^{+/fl}$ mice were crossed with CaMKIIα-Cre mice or injected with AAV5-Ef1F061-Cre-mCherry virus to render all mPFC pyramidal cells heterozygous for *Ank2*. Bottom: max intensity z stack of mCherry fluorescence (red) overlaid with scanning differential interference contrast (DIC) image (grayscale).

(B) Left: two-photon Ca^{2+} transients evoked by bursts of AP doublets in L5 thick-tufted pyramidal neuron dendrites in P52–P67 WT and *Ank2*$^{+/fl}$::CaMKIIα-Cre mice. Right: Ca^{2+} transient amplitude plotted for the first burst (top) and the area under the curve (a.u.c.) of all 5 bursts (bottom) vs. distance. (WT: n = 8, N = 6, *Ank2*$^{+/fl}$-Cre: n = 7, N = 6). Error bars are mean ± SEM. *p < 0.05.

(C) mEPSCs recorded from P54 to P60 WT (black) and *Ank2*$^{+/fl}$-Cre-mCherry-positive (green) neurons. Ticks denote detected events. Left: cumulative probability distribution of mEPSC amplitudes. Distributions were generated per cell, then averaged. Insert: average mEPSC amplitude per cell (WT: −9.4 ± 0.6 pA, n = 14 cells, N = 3 mice; *Ank2*$^{+/fl}$-Cre: −10.1 ± 0.7 pA, n = 15 cells, N = 3 mice) p = 0.5. Right: cumulative probability distribution of mEPSC inter-event intervals (IEI). Insert: average mEPSC frequency per cell (WT: 6.4 ± 1.1 Hz, n = 14 cells; *Ank2*$^{+/fl}$-Cre: 3.3 ± 0.4 Hz, n = 15 cells) *p = 0.01.

(D) Top: paired-pulse ratio of evoked excitatory inputs at 25-, 50-, and 100-ms intervals in P50–P67 WT (black) and *Ank2*$^{+/fl}$-Cre (green) mice. Bottom: PPR grouped by inter-stimulus interval. 25 ms: (WT: 2.0 ± 0.1, n = 10 cells, N = 3 mice; *Ank2*$^{+/fl}$-Cre: 1.6 ± 0.1, n = 11 cells, N = 3 mice) **p = 0.0079. 50 ms: (WT: 1.9±0.1, n = 13 cells; *Ank2*$^{+/fl}$-Cre: 1.5 ± 0.09, n = 11 cells) *p = 0.03. 100 ms: (WT: 1.6 ± 0.1, n = 11 cells; *Ank2*$^{+/fl}$-Cre: 1.3 ± 0.08, n = 12 cells) *p = 0.032.

(E) Top: AMPA-receptor mediated (−80 mV) and mixed AMPA-NMDA (+30) evoked EPSCs from P54 to P60 WT (black) and *Ank2*$^{+/fl}$-Cre-mCherry-positive (green) neurons. Dashed line indicates when NMDA component was calculated (50 ms after stimulation onset). Bottom: quantification of AMPA:NMDA ratio (WT: 3.9 ± 0.6, n = 7 cells, N = 3 mice; *Ank2*$^{+/fl}$-Cre: 2.2 ± 0.2, n = 8 cells, N = 3 mice) **p = 0.009.

(F) Top: voltage-clamp recordings of NMDA receptor-mediated EPSCs at +30 mV in P54–P75 WT (black), *Scn2a*$^{+/-}$ (cyan), *Ank2*$^{+/fl}$-Cre (green) neurons at baseline (dark shade) and after bath application of 1 μM Ro 25-6981 (light shade). Bottom: normalized weighted decay time-constant from baseline and in Ro 25-6981 (WT: 0.898 ± 0.04, n = 11 cells, N = 4 mice; *Scn2a*$^{+/-}$: 0.696 ± 0.02, n = 9 cells, N = 3 mice; *Ank2*$^{+/fl}$-Cre: 0.717 ± 0.03, n = 9 cells, N = 3 mice). WT vs. *Scn2a*$^{+/-}$ ***p = 0.0007; WT vs. *Ank2*$^{+/fl}$-Cre **p = 0.0015; *Scn2a*$^{+/-}$ vs. *Ank2*$^{+/fl}$-Cre p = 0.67.

pyramidal cells. Similar to observations in *Scn2a*$^{+/-}$ cells,[9] spines along apical dendritic shafts had smaller heads relative to their total volume, an anatomical feature typically observed in immature synapses (Figure S8B).

These experiments indicate that ankyrin-B heterozygosity has differential roles in dendritic and axonal compartments, regulating release probability presynaptically and dendritic excitability postsynaptically. But because transmitter release can only be detected at synapses with postsynaptic receptors, the net effect may be a reduction in excitatory transmission. To test this, we first isolated the postsynaptic contributions of ankyrin-B and compared them to loss in both pre- and postsynaptic compartments. A dilute AAV-EF1α-Cre-mCherry virus was injected into the medial prefrontal cortex (mPFC) of *Ank2*$^{+/fl}$ mice at P30 to render only a few cells heterozygous for *Ank2* (Figure 7A). In these conditions, cell-autonomous effects of *Ank2*

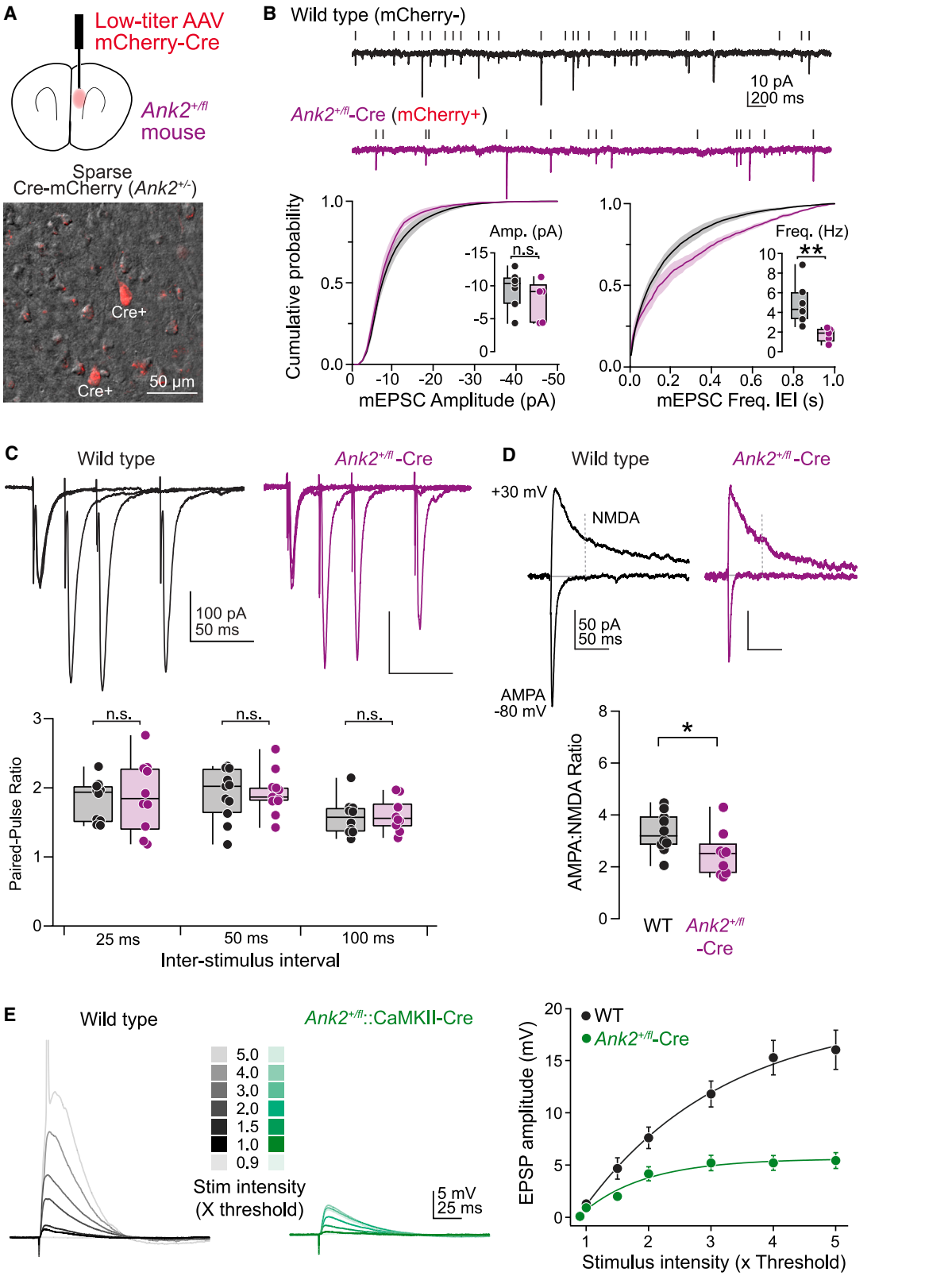

(legend on next page)

haploinsufficiency in dendrites could be assessed by recording from one of the few mCherry-positive neurons that receive input from largely mCherry-negative (e.g., WT) inputs (Figure 7A). Consistent with a lack of presynaptic effect in this experimental design, PPR was not different between mCherry-positive and -negative cells (Figure 7C), and matched PPR values obtained from uninfected WT littermates (Figure 6E). By contrast, postsynaptic components of transmission were affected to the same degree as those observed in *Ank2*$^{+/fl}$::CaMKII-Cre conditions. The sparsely labeled Cre-positive *Ank2* heterozygous neurons showed a reduction in mEPSC frequency and in the AMPA:NMDA ratio compared with interleaved Cre-negative neurons recorded in the same slice (Figures 7B and 7D). The relative reduction in mEPSC frequency and AMPA:NMDA ratio, normalized to each condition's WT comparison, was no different between full conditional *Ank2* heterozygosity, cell-autonomous postsynaptic *Ank2* heterozygosity, or prior experiments focused on *Scn2a* heterozygosity (AMPA:NMDA ratio [norm. to WT avg.]: *Ank2*$^{+/fl}$-Cre high-titer: 0.57 ± 0.06 n = 8 cells; *Ank2*$^{+/fl}$-Cre low-titer: 0.74 ± 0.09, n = 9 cells; *Scn2a*$^{+/-}$: 0.6 ± 0.09, n = 11 cells. No significant differences. mEPSC frequency [norm. to WT avg.]: *Ank2*$^{+/fl}$-Cre high-titer: 0.52 ± 0.07 n = 15 cells; *Ank2*$^{+/fl}$-Cre low-titer: 0.35 ± 0.07, n = 5 cells; *Scn2a*$^{+/-}$: 0.5 ± 0.09, n = 19 cells. No significant differences).

Taken together, these experiments suggest that the postsynaptic effects of *Ank2* heterozygosity impair excitatory transmission, despite an apparent increase in presynaptic release probability. To test this directly, we returned to *Ank2*$^{+/fl}$::CaMKII-Cre mice and assessed excitatory transmission across a range of stimulus intensities, from threshold for excitatory postsynaptic potential (EPSP) generation to 5× that threshold. In WT neurons, increased stimulation intensity increased EPSP amplitude to levels where many cells fired APs. By contrast, a higher stimulus intensity was required to evoke EPSPs in *Ank2*$^{+/-}$-Cre neurons (threshold voltage: WT: 4.9 ± 0.3 V, *Ank2*$^{+/-}$: 7.8 ± 0.4 V; n = 8 cells each), and resultant EPSPs were far smaller (Figure 7E).

What might be a mechanism for these changes in synaptic efficacy? Backpropagating APs provide instructive signals to the dendrites that are necessary to maintain synaptic strength, integration, and plasticity. We hypothesized that reductions in bAP efficacy in *Ank2* haploinsufficient neurons, due to disruptions in Na_V dendritic localization, could impair activity-dependent synaptic plasticity. We tested this by pairing bursts of APs, which backpropagate poorly in *Ank2*$^{+/-}$ neurons (Figure 6), with synaptic inputs impinging upon the apical tuft of L5 pyramidal neurons (Figure 8A, EPSP preceding APs by ∼10 ms). In WT conditions, this pairing evoked long-term potentiation (LTP) reliably in mice aged <P25. Therefore, to test this in *Ank2*$^{+/-}$ neurons, we crossed *Ank2*$^{+/fl}$ mice to Rbp4-Cre-Ai14 driver lines, as this allows for expression of Cre in L5 pyramidal cells during early embryonic development (E13.5).[58,59] As in prior studies in *Scn2a*$^{+/-}$ neurons, LTP could not be induced in *Ank2*$^{+/-}$ cells (Figures 8B–8D). Altogether, these results indicate that ankyrin-B has a critical role in the scaffolding of dendritic Na_Vs and that *Ank2* haploinsufficiency phenocopies postsynaptic dendritic deficits observed in *Scn2a*$^{+/-}$ neurons.

DISCUSSION

Ankyrin-B variants have long been known to contribute to cardiac dysfunction through their function in scaffolding a range of membrane pumps, ion exchangers, and receptors.[60] Here, we provide evidence that ankyrin-B (*Ank2*) functions as the primary scaffold for $Na_V1.2$ (*Scn2a*) in the dendrites of neocortical pyramidal neurons. Haploinsufficiency of *Ank2* in prefrontal neocortical neurons caused dendritic excitability and synaptic deficits due to reduced Na_V channel density within the dendritic membrane, which phenocopies *Scn2a* haploinsufficient conditions. These findings establish a direct, convergent mechanism between two major ASD-associated genes and add to a growing body of literature demonstrating dysfunction in dendritic excitability in ASD.[61–64]

Subcellular patterning of ankyrins

Although ion channels and ankyrin scaffold interactions have been studied extensively in axonal domains,[13,65–68] the mechanisms governing dendritic localization of Na_Vs have received far less attention. Data here suggest that ankyrin-G and ankyrin-B have largely distinct roles in Na_V scaffolding, with ankyrin-G localized to excitable parts of the axon (e.g., AIS and nodes of Ranvier), and ankyrin-B localized to other regions, including dendrites. We show that ankyrin-B is critical for scaffolding $Na_V1.2$ to the dendritic shaft. Consistent with this, knockout of ankyrin-B in cultured neurons eliminates dendritic $Na_V1.2$ immunostaining (Figures 1 and S4), and *Ank2*$^{+/-}$ conditions decrease AP-evoked dendritic Na^+ influx by ∼50% (Figure 5). Interestingly, ankyrin-G is known to localize within spines, but does so in support of synapse function rather than Na_V scaffolding.[39] Together, this suggests that dendritic sodium channels are scaffolded exclusively by ankyrin-B and that loss of ankyrin-B cannot be compensated for by other ankyrins.

Figure 7. Cell-autonomous *Ank2* haploinsufficiency results in postsynaptic excitatory synaptic dysfunction

(A) Top: neurons were sparsely transduced by injecting a diluted AAV5-Ef1α-Cre-mCherry virus in mPFC of P30 *Ank2*$^{+/fl}$ mice. Bottom: max intensity z stack of mCherry fluorescence (red) overlaid with scanning DIC image (grayscale) showing Ef1α-Cre-mCherry expression in a subset of *Ank2*$^{+/fl}$ L5 pyramidal neurons.

(B) mEPSCs from P55 to P65 interleaved mCherry-negative (black) or *Ank2*$^{+/fl}$-Cre-mCherry-positive (purple) neurons. Data quantified as in Figure 6C. mEPSC amplitude: mCherry−: −9.5 ± 1.1 pA, n = 7 cells, N = 3 mice; mCherry+: −7.7 ± 1.4 pA, n = 5 cells, N = 3 mice; p = 0.43. mEPSC frequency: mCherry−: 4.9 ± 0.8 Hz, n = 7 cells; *Ank2*$^{+/fl}$-Cre: 1.7 ± 0.3 Hz, n = 5 cells; **p = 0.0025.

(C) Paired-pulse ratio from P52 to P73 WT (black) and *Ank2*$^{+/fl}$-Cre-mCherry (purple) neurons, shown as in Figure 6D. PPR at 25 ms: (WT: 1.8 ± 0.1, n = 10 cells, N = 5 mice; *Ank2*$^{+/fl}$-Cre: 1.9 ± 0.2, n = 10 cells, N = 3 mice) p > 0.99. At 50 ms: (WT: 1.9 ± 0.1, n = 11 cells; *Ank2*$^{+/fl}$-Cre: 1.9 ± 0.1, n = 11 cells) p = 0.7. At 100 ms: (WT: 1.6 ± 0.9, n = 10 cells; *Ank2*$^{+/fl}$-Cre: 1.6 ± 0.07, n = 10 cells) p = 0.6.

(D) AMPA:NMDA ratio from P52 to P73 WT (black) and *Ank2*$^{+/fl}$-Cre-mCherry (purple) neurons, as in Figure 6E (WT: 3.3 ± 0.2, n = 10 cells, N = 5 mice; *Ank2*$^{+/fl}$-Cre: 2.5 ± 0.3, n = 9 cells, N = 3 mice) *p = 0.02.

(E) Left: evoked EPSPs in response to incremental increases in stimulus intensity in P85–P93 WT (black) and *Ank2*$^{+/fl}$::CaMKIIα-Cre mice (green). Right: input-output curves of EPSP amplitude vs. stimulus intensity as a factor of threshold intensity. Circles are mean ± SEM. Line is exponential fit. n = 9 WT, 8 *Ank2*$^{+/fl}$.

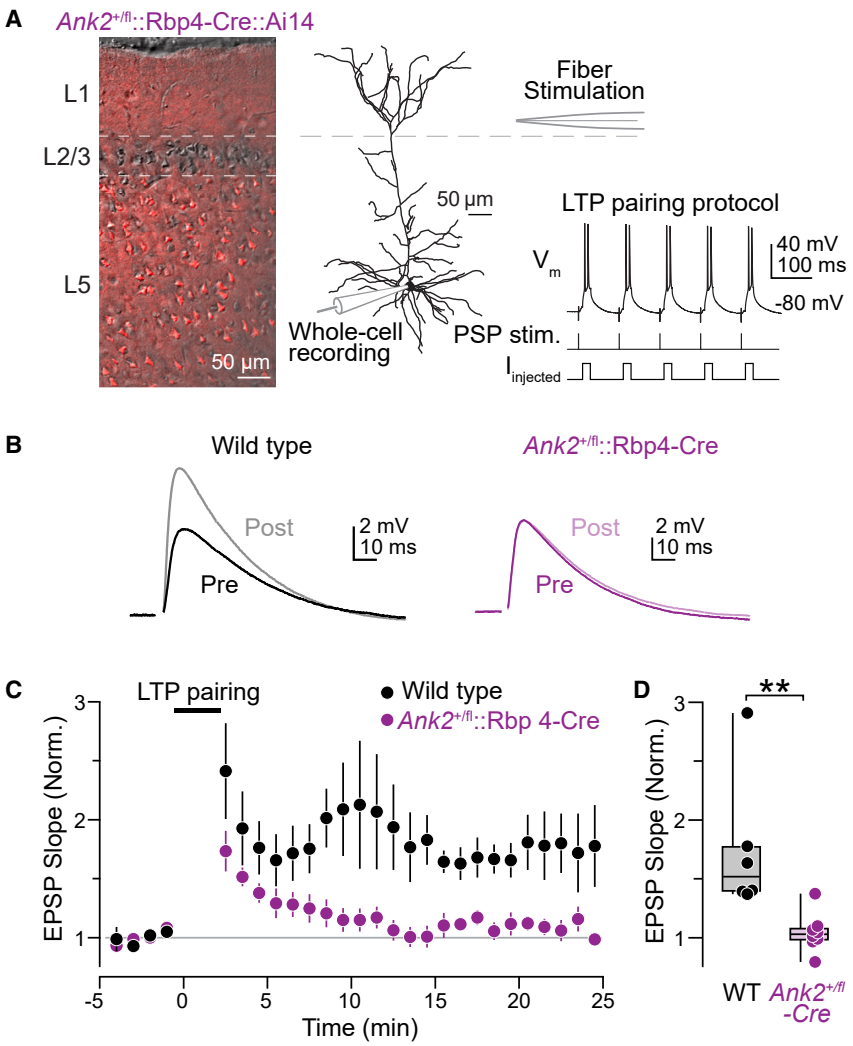

Figure 8. *Ank2* haploinsufficiency impairs synaptic plasticity

(A) Single two-photon optical section of Ai14-tdTomato fluorescence (red) overlaid with scanning DIC image (grayscale) showing expression of Rbp4-Cre in L5 pyramidal neurons in the mPFC of a P26 *Ank2*$^{+/fl}$::Rbp4-Cre-Ai14 mouse. Right: recording configuration to induce burst-dependent long-term potentiation (LTP) in L5 pyramidal neurons. A stimulating electrode was placed in L1 and synaptic stimulation was paired with bursts of APs evoked by depolarization from the somatic pipette.

(B) EPSPs before (dark) and after (light) the LTP pairing protocol from P17 to P23 WT (black) and *Ank2*$^{+/fl}$::Rbp4-Cre (purple) mice. Lighter shades represent data 20–25 min after pairing.

(C) EPSP slope (first 2 ms) vs. time before and after LTP induction. Circle and bars are mean ± SEM.

(D) Average EPSP slope per cell 20–25 min post-induction from WT and *Ank2*$^{+/fl}$::Rbp4-Cre neurons (WT: 1.75 ± 0.2, n = 6 cells, N = 2 mice; *Ank2*$^{+/fl}$-Cre: 1.05 ± 0.06, n = 8 cells, N = 2 mice) **p = 0.001.

Intriguingly, one place where ankyrin-B and ankyrin-G overlap, and appear to serve compensatory Na_V scaffolding roles, is at the somatic membrane. Here, we observed a disconnect between *Ank2*$^{+/-}$ and *Scn2a*$^{+/-}$ conditions, as *Ank2*$^{+/-}$ neurons did not show a decrease in peak AP velocity common to *Scn2a*$^{+/-}$ neurons[9,26] (Figure 4). This indicates that somatic Na_Vs can be scaffolded at the soma at WT levels in *Ank2*$^{+/-}$ conditions, either by ankyrin-G or by preferential recruitment of extant ankyrin-B to the soma over other compartments. In support of the former, we found that $Na_V1.2$-3xFLAG constructs were still present at the soma in *Ank2*$^{-/-}$ cultured neurons, despite being absent from dendrites (Figure 4). Methods to label each ankyrin, their splice variants, and Na_V subtypes scaffolded within each of these compartments in neurons will be useful to unravel these complexities.

Although it appears that both ankyrins can scaffold somatic Na_Vs, it remains unclear why they fail to compensate for one another outside the soma. One explanation may lie in how ankyrin-G and ankyrin-B are themselves localized to different neuronal compartments. Previous studies have shown that ankyrin-G requires the post-translational modification *S*-palmitoylation for its membrane association at the AIS.[69] *S*-palmitoylation is mediated by a family of 23 palmitoyl acyl transferases (zDHHC PATs), which covalently adds a 16-carbon fatty acid chain to a conserved cysteine 70 (C70) that resides within the ankyrin repeats.[70] Two of these PATs, zDHHC5 and zDHHC8, are known to palmitoylate ankyrin-G at the AIS.[69] By contrast, ankyrin-B is palmitoylated at multiple cysteine residues by a distinct PAT, zDHHC17, and this *S*-palmitoylation is necessary for dendritic scaffolding of $Na_V1.2$.[71]

In addition to differential localization of ankyrin family members, individual splice variants of ankyrin-G and ankyrin-B have unique localization patterns and functions. Alternative splicing of *ANK2* gives rise to two main isoforms of ankyrin-B in the brain: a canonical 220-kDa isoform and a larger 440-kDa splice variant that contains a single 6.4-kb neuron-specific exon within the middle of the gene.[72–74] Here, we found that the 220-kDa ankyrin-B is expressed throughout dendrites, whereas the 440-kDa isoform was dominant in distal axons (Figure 2). Using conditional *Ank2* alleles, we removed *Ank2* from prefrontal pyramidal cells to isolate the cell-autonomous, postsynaptic roles of the 220-kDa isoform and found that it is capable of scaffolding $Na_V1.2$ through direct interaction. This impaired dendritic excitability and excitatory synaptic function in ways that converged with those observed in *Scn2a*$^{+/-}$ neurons.[9] Although these effects likely contribute to ASD etiology, ASD-associated variants in *ANK2* cannot only affect the 220-kDa ankyrin-B, as the 440-kDa isoform will also be impacted. Most variants in *ANK2* fall into this category, resulting in heterozygous expression and haploinsufficiency of both the 220- and 440-kDa isoforms in humans.[6,8] Nevertheless, three ASD-associated variants have been identified in the neuronal-specific exon in *ANK2*,

which is only found within the 440-kDa isoform.[38] Here, we found that a modest decrease in PPR was likely attributed to heterozygous loss of axonal *Ank2*, similar to reports examining a frameshift variant at R2608 that specifically affects the 440-kDa isoform.[38] How axonal ankyrin-B heterozygosity alters short-term plasticity is unclear but, in the heart, *Ank2*$^{+/-}$ enhances calcium release from intracellular stores.[75] Such mechanisms, if engaged at axonal boutons, could affect neurotransmitter release.[76] Therefore, changes in the 440-kDa ankyrin-B, which is predominantly found within the distal axon, could lead to altered presynaptic neurotransmitter release.

Convergent dendritic dysfunction in ASD

Dysfunction in L5 neocortical pyramidal cells has long been implicated in ASD.[10] These neurons have a unique structure, with a set of basal and apical dendrites that arborize to receive distinct inputs from local and long-range sources, respectively.[77] Dendritic integration, including supralinear dendritic spikes in the apical tuft, are thought to support several computations, including sensory integration, binding of local and long-range input streams, and top-down modulation of cortical processing.[78–84] Indeed, these aspects of dendritic excitability are critical for detection of sensory stimuli at the behavioral threshold[85–88] and are some of the first neuronal signals affected with anesthesia-induced loss of consciousness.[89] Given these major roles in higher-order cortical processing, it is likely that dysfunction in dendritic integration is an important contributor to neurodevelopmental disorders like ASD and intellectual disability (ID). Consistent with this, *Scn2a* haploinsufficiency, which principally interferes with dendritic excitability in neocortex, confers substantial risk for ASD.[4,6–8] We find that *Ank2* converges with *Scn2a* to affect the same dendritic excitability mechanisms. This convergence is direct, as ankyrin-B is the obligate scaffold for dendritic $Na_V1.2$. Emerging evidence indicates that other ASD-associated genes may similarly affect neocortical pyramidal cell dendritic integration, either via regulation of Na_Vs,[62] other channels that influence dendritic excitability,[90–95] or changes in excitation that promote dendritic non-linear events or inhibition that limits such activity.[96–100] These effects can be overt, with ASD-associated variants directly affecting genes encoding dendritic or synaptic proteins in question, or covert, with ASD-associated variants instead affecting gene regulatory elements that, in turn, alter protein expression (reviewed in Nelson and Bender[64]).

$Na_V1.2$ is critical for dendritic excitability throughout life. Conditionally induced heterozygosity of *Scn2a* late in development results in identical impairments in dendritic and synaptic function, as observed in constitutive *Scn2a* heterozygotes.[9] Excitatory synapses appear similar to those found in immature neurons, with relatively small spine heads and low AMPA:NMDA receptor ratios, suggesting that synapses may be maintained in an immature, pre-critical-period state.[9] Indeed, restoration of near-WT levels of *Scn2a*, either via Cre-induced genetic rescue or CRISPR-activator-based upregulation of the residual, functional allele in *Scn2a* heterozygotes, restores dendritic excitability and synapse function to WT levels.[43] This suggests that restoration of *Ank2* function would have similar benefits, at least in dendritic regions where it actively scaffolds $Na_V1.2$. *ANK* genes are too large for traditional gene therapy approaches; however, several other approaches are maturing for gene regulation in neurodevelopmental disorders, with marked progress for a number of genetic conditions.[43,101–106] In addition, a better understanding of the unique roles of different ankyrin isoforms in scaffolding and function of various binding partners[96,98–100] may provide insight into methods that allow ankyrins to better compensate for one another in dendritic compartments. Overall, these data establish a framework in which both *Scn2a*$^{+/-}$ and *Ank2*$^{+/-}$ models are forms of channelopathies contributing to ASD,[107] motivating future research on potential convergent impairments in channel and dendritic function associated with other ASD/ID risk genes.

Complex physiology of ankyrin-B dysfunction

Outside the brain, ankyrin-B is most highly expressed in the heart. Here, *ANK2* variants are associated with ankyrin-B syndrome, a complex cardiovascular phenotype that can lead to sudden cardiac death.[52] Currently, it is unclear whether patients with *ANK2* missense or protein truncating variants will develop either ASD/ID, cardiovascular disorders, or both, perhaps at different points in development. One of the major challenges to linking *ANK2* variants to specific disease phenotypes is that, even within cohorts that share the same variant, cardiac phenotypes can range from asymptomatic to long-QT syndrome to sudden cardiac arrest.[108,109] In addition, in our prior work on genotype-phenotype relationships in *SCN2A*,[7,110] we encountered challenges in obtaining full neurological and physiological reports, including seizure status, from clinicians. In *ANK2*, similar challenges are apparent between brain and cardiac specialists, compounded by the observation that most neuropsychiatric phenotypes have been reported in children, whereas most cardiac phenotypes have been reported in adults. Finally, although ankyrin-B clearly plays an important role in both the heart and the brain, the resultant clinical phenotype of disease-associated variation is likely to depend on which isoforms of ankyrin-B are affected, the nature and severity of the variant (i.e., missense vs. protein-truncating), and the specific effects of missense variants on binding to tissue-specific partners. Future clinical and basic science studies exploring the myriad roles of *ANK2* will therefore need to consider its complex actions in diverse systems.

STAR★METHODS

Detailed methods are provided in the online version of this paper and include the following:

- KEY RESOURCES TABLE
- RESOURCE AVAILABILITY
  - Lead contact
  - Materials availability
  - Data and code availability
- EXPERIMENTAL MODEL AND STUDY PARTICIPANT DETAILS
  - Mouse strains
- METHOD DETAILS
  - Constructs, antibodies, and experimental models

- Co-immunoprecipitation
- Western blot
- Proximity ligation assay
- Neocortical cultures, transfections, and immunofluorescence
- Confocal microscopy
- *In vitro* cell electrophysiology
- Compartmental modeling
- *Ex vivo* electrophysiology
- Two-photon imaging

- QUANTIFICATION AND STATISTICAL ANALYSIS

SUPPLEMENTAL INFORMATION

Supplemental information can be found online at https://doi.org/10.1016/j.neuron.2024.01.003.

ACKNOWLEDGMENTS

We are grateful to members of the Jenkins and Bender labs and Drs. L. Isom, M. Roberts, and L. Ptáček for comments and feedback. We thank Dr. M. Roberts for help with analysis code related to Figure 4H. This work was supported by the Rackham Predoctoral Fellowship (J.P.G.), Simons Foundation SFARI 675594 (P.M.J.), and NIH grants T32GM007315 (K.P.D. and C.C.E.), F32MH125536 and K99MH135209 (A.D.N.), R01MH126960 (P.M.J. and K.J.B.), and R01MH125978 (K.J.B.).

AUTHOR CONTRIBUTIONS

S.J.S., K.J.B., and P.M.J. conceived the project. A.D.N., A.M.C., J.P.G., L.M., R.N.C.-F., K.P.D., C.C.E., A.S., K.D.D., H.K., K.J.B., and P.M.J. designed and performed experiments and analyzed the data. A.D.N. wrote the manuscript. A.D.N., K.J.B., and P.M.J. edited the manuscript.

DECLARATION OF INTERESTS

K.J.B. and S.J.S. receive research funding from BioMarin Pharmaceutical Inc. K.J.B. is on the SAB for Regel Tx and receives research support from Regel Tx.

Received: June 8, 2022
Revised: April 26, 2023
Accepted: January 3, 2024
Published: January 29, 2024

REFERENCES

1. Iossifov, I., O'Roak, B.J., Sanders, S.J., Ronemus, M., Krumm, N., Levy, D., Stessman, H.A., Witherspoon, K.T., Vives, L., Patterson, K.E., et al. (2014). The contribution of de novo coding mutations to autism spectrum disorder. Nature *515*, 216–221.
2. Neale, B.M., Kou, Y., Liu, L., Ma'ayan, A., Samocha, K.E., Sabo, A., Lin, C.F., Stevens, C., Wang, L.S., Makarov, V., et al. (2012). Patterns and rates of exonic de novo mutations in autism spectrum disorders. Nature *485*, 242–245.
3. O'Roak, B.J., Vives, L., Fu, W., Egertson, J.D., Stanaway, I.B., Phelps, I.G., Carvill, G., Kumar, A., Lee, C., Ankenman, K., et al. (2012). Multiplex targeted sequencing identifies recurrently mutated genes in autism spectrum disorders. Science *338*, 1619–1622.
4. Sanders, S.J., Murtha, M.T., Gupta, A.R., Murdoch, J.D., Raubeson, M.J., Willsey, A.J., Ercan-Sencicek, A.G., DiLullo, N.M., Parikshak, N.N., Stein, J.L., et al. (2012). De novo mutations revealed by whole-exome sequencing are strongly associated with autism. Nature *485*, 237–241.
5. Sanders, S.J., He, X., Willsey, A.J., Ercan-Sencicek, A.G., Samocha, K.E., Cicek, A.E., Murtha, M.T., Bal, V.H., Bishop, S.L., Dong, S., et al. (2015). Insights into Autism Spectrum Disorder Genomic Architecture and Biology from 71 Risk Loci. Neuron *87*, 1215–1233.
6. Satterstrom, F.K., Kosmicki, J.A., Wang, J., Breen, M.S., De Rubeis, S., An, J.Y., Peng, M., Collins, R., Grove, J., Klei, L., et al. (2020). Large-Scale Exome Sequencing Study Implicates Both Developmental and Functional Changes in the Neurobiology of Autism. Cell *180*, 568–584.e23.
7. Ben-Shalom, R., Keeshen, C.M., Berrios, K.N., An, J.Y., Sanders, S.J., and Bender, K.J. (2017). Opposing Effects on $Na_V1.2$ Function Underlie Differences Between SCN2A Variants Observed in Individuals With Autism Spectrum Disorder or Infantile Seizures. Biol. Psychiatry *82*, 224–232.
8. Fu, J.M., Satterstrom, F.K., Peng, M., Brand, H., Collins, R.L., Dong, S., Wamsley, B., Klei, L., Wang, L., Hao, S.P., et al. (2022). Rare coding variation provides insight into the genetic architecture and phenotypic context of autism. Nat. Genet. *54*, 1320–1331.
9. Spratt, P.W.E., Ben-Shalom, R., Keeshen, C.M., Burke, K.J., Jr., Clarkson, R.L., Sanders, S.J., and Bender, K.J. (2019). The Autism-Associated Gene Scn2a Contributes to Dendritic Excitability and Synaptic Function in the Prefrontal Cortex. Neuron *103*, 673–685.e5.
10. Willsey, A.J., Sanders, S.J., Li, M., Dong, S., Tebbenkamp, A.T., Muhle, R.A., Reilly, S.K., Lin, L., Fertuzinhos, S., Miller, J.A., et al. (2013). Coexpression networks implicate human midfetal deep cortical projection neurons in the pathogenesis of autism. Cell *155*, 997–1007.
11. Bennett, V., and Lorenzo, D.N. (2016). An Adaptable Spectrin/Ankyrin-Based Mechanism for Long-Range Organization of Plasma Membranes in Vertebrate Tissues. Curr. Top. Membr. *77*, 143–184.
12. Lemaillet, G., Walker, B., and Lambert, S. (2003). Identification of a conserved ankyrin-binding motif in the family of sodium channel alpha subunits. J. Biol. Chem. *278*, 27333–27339.
13. Nelson, A.D., and Jenkins, P.M. (2017). Axonal Membranes and Their Domains: Assembly and Function of the Axon Initial Segment and Node of Ranvier. Front. Cell. Neurosci. *11*, 136.
14. Jenkins, P.M., Kim, N., Jones, S.L., Tseng, W.C., Svitkina, T.M., Yin, H.H., and Bennett, V. (2015). Giant ankyrin-G: a critical innovation in vertebrate evolution of fast and integrated neuronal signaling. Proc. Natl. Acad. Sci. USA *112*, 957–964.
15. Jenkins, S.M., and Bennett, V. (2001). Ankyrin-G coordinates assembly of the spectrin-based membrane skeleton, voltage-gated sodium channels, and L1 CAMs at Purkinje neuron initial segments. J. Cell Biol. *155*, 739–746.
16. Pan, Z., Kao, T., Horvath, Z., Lemos, J., Sul, J.Y., Cranstoun, S.D., Bennett, V., Scherer, S.S., and Cooper, E.C. (2006). A common ankyrin-G-based mechanism retains KCNQ and NaV channels at electrically active domains of the axon. J. Neurosci. *26*, 2599–2613.
17. Zhou, D., Lambert, S., Malen, P.L., Carpenter, S., Boland, L.M., and Bennett, V. (1998). AnkyrinG is required for clustering of voltage-gated Na channels at axon initial segments and for normal action potential firing. J. Cell Biol. *143*, 1295–1304.
18. Lorenzo, D.N., Badea, A., Davis, J., Hostettler, J., He, J., Zhong, G., Zhuang, X., and Bennett, V. (2014). A PIK3C3-ankyrin-B-dynactin pathway promotes axonal growth and multiorganelle transport. J. Cell Biol. *207*, 735–752.
19. Inda, M.C., DeFelipe, J., and Muñoz, A. (2006). Voltage-gated ion channels in the axon initial segment of human cortical pyramidal cells and their relationship with chandelier cells. Proc. Natl. Acad. Sci. USA *103*, 2920–2925.
20. Boiko, T., Van Wart, A., Caldwell, J.H., Levinson, S.R., Trimmer, J.S., and Matthews, G. (2003). Functional specialization of the axon initial segment by isoform-specific sodium channel targeting. J. Neurosci. *23*, 2306–2313.
21. Gazina, E.V., Leaw, B.T., Richards, K.L., Wimmer, V.C., Kim, T.H., Aumann, T.D., Featherby, T.J., Churilov, L., Hammond, V.E., Reid,

C.A., et al. (2015). 'Neonatal' Nav1.2 reduces neuronal excitability and affects seizure susceptibility and behaviour. Hum. Mol. Genet. *24*, 1457–1468.

22. O'Brien, J.E., and Meisler, M.H. (2013). Sodium channel SCN8A (Nav1.6): properties and de novo mutations in epileptic encephalopathy and intellectual disability. Front. Genet. *4*, 213.
23. Van Wart, A., Trimmer, J.S., and Matthews, G. (2007). Polarized distribution of ion channels within microdomains of the axon initial segment. J. Comp. Neurol. *500*, 339–352.
24. Hu, W., Tian, C., Li, T., Yang, M., Hou, H., and Shu, Y. (2009). Distinct contributions of Na(v)1.6 and Na(v)1.2 in action potential initiation and backpropagation. Nat. Neurosci. *12*, 996–1002.
25. Lorincz, A., and Nusser, Z. (2010). Molecular identity of dendritic voltage-gated sodium channels. Science *328*, 906–909.
26. Spratt, P.W.E., Alexander, R.P.D., Ben-Shalom, R., Sahagun, A., Kyoung, H., Keeshen, C.M., Sanders, S.J., and Bender, K.J. (2021). Paradoxical hyperexcitability from $Na_V1.2$ sodium channel loss in neocortical pyramidal cells. Cell Rep. *36*, 109483.
27. Zhang, J., Chen, X., Eaton, M., Wu, J., Ma, Z., Lai, S., Park, A., Ahmad, T.S., Que, Z., Lee, J.H., et al. (2021). Severe deficiency of the voltage-gated sodium channel $Na_V1.2$ elevates neuronal excitability in adult mice. Cell Rep. *36*, 109495.
28. Boiko, T., Rasband, M.N., Levinson, S.R., Caldwell, J.H., Mandel, G., Trimmer, J.S., and Matthews, G. (2001). Compact myelin dictates the differential targeting of two sodium channel isoforms in the same axon. Neuron *30*, 91–104.
29. Liu, H., Wang, H.G., Pitt, G.S., and Liu, Z.J. (2022). Direct Observation of Compartment-Specific Localization and Dynamics of Voltage-Gated Sodium Channels. J. Neurosci. *42*, 5482–5498.
30. Yamano, R., Miyazaki, H., and Nukina, N. (2022). The diffuse distribution of Nav1.2 on mid-axonal regions is a marker for unmyelinated fibers in the central nervous system. Neurosci. Res. *177*, 145–150.
31. Roberts, J.D., Murphy, N.P., Hamilton, R.M., Lubbers, E.R., James, C.A., Kline, C.F., Gollob, M.H., Krahn, A.D., Sturm, A.C., Musa, H., et al. (2019). Ankyrin-B dysfunction predisposes to arrhythmogenic cardiomyopathy and is amenable to therapy. J. Clin. Invest. *129*, 3171–3184.
32. Cai, X., and Zhang, Y. (2006). Molecular evolution of the ankyrin gene family. Mol. Biol. Evol. *23*, 550–558.
33. Wang, C., Wei, Z., Chen, K., Ye, F., Yu, C., Bennett, V., and Zhang, M. (2014). Structural basis of diverse membrane target recognitions by ankyrins. eLife *3*, e04353.
34. Gao, Y., Hisey, E., Bradshaw, T.W.A., Erata, E., Brown, W.E., Courtland, J.L., Uezu, A., Xiang, Y., Diao, Y., and Soderling, S.H. (2019). Plug-and-Play Protein Modification Using Homology-Independent Universal Genome Engineering. Neuron *103*, 583–597.e8.
35. Wu, H.C., Yamankurt, G., Luo, J., Subramaniam, J., Hashmi, S.S., Hu, H., and Cunha, S.R. (2015). Identification and characterization of two ankyrin-B isoforms in mammalian heart. Cardiovasc. Res. *107*, 466–477.
36. Cunha, S.R., Le Scouarnec, S., Schott, J.J., and Mohler, P.J. (2008). Exon organization and novel alternative splicing of the human ANK2 gene: implications for cardiac function and human cardiac disease. J. Mol. Cell. Cardiol. *45*, 724–734.
37. Creighton, B.A., Afriyie, S., Ajit, D., Casingal, C.R., Voos, K.M., Reger, J., Burch, A.M., Dyne, E., Bay, J., Huang, J.K., et al. (2021). Giant ankyrin-B mediates transduction of axon guidance and collateral branch pruning factor sema 3A. eLife *10*, e69815.
38. Yang, R., Walder-Christensen, K.K., Kim, N., Wu, D., Lorenzo, D.N., Badea, A., Jiang, Y.H., Yin, H.H., Wetsel, W.C., and Bennett, V. (2019). ANK2 autism mutation targeting giant ankyrin-B promotes axon branching and ectopic connectivity. Proc. Natl. Acad. Sci. USA *116*, 15262–15271.
39. Smith, K.R., Kopeikina, K.J., Fawcett-Patel, J.M., Leaderbrand, K., Gao, R., Schürmann, B., Myczek, K., Radulovic, J., Swanson, G.T., and Penzes, P. (2014). Psychiatric risk factor ANK3/ankyrin-G nanodomains regulate the structure and function of glutamatergic synapses. Neuron *84*, 399–415.
40. Garrido, J.J., Giraud, P., Carlier, E., Fernandes, F., Moussif, A., Fache, M.P., Debanne, D., and Dargent, B. (2003). A targeting motif involved in sodium channel clustering at the axonal initial segment. Science *300*, 2091–2094.
41. Tseng, W.C., Jenkins, P.M., Tanaka, M., Mooney, R., and Bennett, V. (2015). Giant ankyrin-G stabilizes somatodendritic GABAergic synapses through opposing endocytosis of GABAA receptors. Proc. Natl. Acad. Sci. USA *112*, 1214–1219.
42. Nelson, A.D., Caballero-Florán, R.N., Rodríguez Díaz, J.C., Hull, J.M., Yuan, Y., Li, J., Chen, K., Walder, K.K., Lopez-Santiago, L.F., Bennett, V., et al. (2020). Ankyrin-G regulates forebrain connectivity and network synchronization via interaction with GABARAP. Mol. Psychiatry *25*, 2800–2817.
43. Tamura, S., Nelson, A.D., Spratt, P.W.E., Kyoung, H., Zhou, X., Li, Z., Zhao, J., Holden, S.S., Sahagun, A., Keeshen, C.M., et al. (2022). CRISPR activation rescues abnormalities in SCN2A haploinsufficiency-associated autism spectrum disorder. Preprint at bioRxiv.
44. Xu, B., Zang, K., Ruff, N.L., Zhang, Y.A., McConnell, S.K., Stryker, M.P., and Reichardt, L.F. (2000). Cortical degeneration in the absence of neurotrophin signaling: dendritic retraction and neuronal loss after removal of the receptor TrkB. Neuron *26*, 233–245.
45. Blömer, L.A., Canepari, M., and Filipis, L. (2021). Ultrafast Sodium Imaging of the Axon Initial Segment of Neurons in Mouse Brain Slices. Curr. Protoc. *1*, e64.
46. Filipis, L., and Canepari, M. (2021). Optical measurement of physiological sodium currents in the axon initial segment. J. Physiol. *599*, 49–66.
47. Lipkin, A.M., Cunniff, M.M., Spratt, P.W.E., Lemke, S.M., and Bender, K.J. (2021). Functional Microstructure of Ca_V-Mediated Calcium Signaling in the Axon Initial Segment. J. Neurosci. *41*, 3764–3776.
48. Choi, C.S.W., Souza, I.A., Sanchez-Arias, J.C., Zamponi, G.W., Arbour, L.T., and Swayne, L.A. (2019). Ankyrin B and Ankyrin B variants differentially modulate intracellular and surface Cav2.1 levels. Mol. Brain *12*, 75.
49. Garcia-Caballero, A., Zhang, F.X., Hodgkinson, V., Huang, J., Chen, L., Souza, I.A., Cain, S., Kass, J., Alles, S., Snutch, T.P., et al. (2018). T-type calcium channels functionally interact with spectrin (α/β) and ankyrin B. Mol Brain. Mol. Brain *11*, 24.
50. Kline, C.F., Scott, J., Curran, J., Hund, T.J., and Mohler, P.J. (2014). Ankyrin-B regulates Cav2.1 and Cav2.2 channel expression and targeting. J. Biol. Chem. *289*, 5285–5295.
51. Chalifoux, J.R., and Carter, A.G. (2011). GABAB receptor modulation of voltage-sensitive calcium channels in spines and dendrites. J. Neurosci. *31*, 4221–4232.
52. Koenig, S.N., and Mohler, P.J. (2017). The evolving role of ankyrin-B in cardiovascular disease. Heart Rhythm *14*, 1884–1889.
53. Gulledge, A.T., and Stuart, G.J. (2003). Action potential initiation and propagation in layer 5 pyramidal neurons of the rat prefrontal cortex: absence of dopamine modulation. J. Neurosci. *23*, 11363–11372.
54. Short, S.M., Oikonomou, K.D., Zhou, W.L., Acker, C.D., Popovic, M.A., Zecevic, D., and Antic, S.D. (2017). The stochastic nature of action potential backpropagation in apical tuft dendrites. J. Neurophysiol. *118*, 1394–1414.
55. Stuart, G.J., and Häusser, M. (2001). Dendritic coincidence detection of EPSPs and action potentials. Nat. Neurosci. *4*, 63–71.
56. Larkum, M.E., Kaiser, K.M., and Sakmann, B. (1999). Calcium electrogenesis in distal apical dendrites of layer 5 pyramidal cells at a critical frequency of back-propagating action potentials. Proc. Natl. Acad. Sci. USA *96*, 14600–14604.
57. France, G., Fernández-Fernández, D., Burnell, E.S., Irvine, M.W., Monaghan, D.T., Jane, D.E., Bortolotto, Z.A., Collingridge, G.L., and Volianskis, A. (2017). Multiple roles of GluN2B-containing NMDA

receptors in synaptic plasticity in juvenile hippocampus. Neuropharmacology *112*, 76–83.

58. Fazel Darbandi, S., Nelson, A.D., Pai, E.L., Bender, K.J., and Rubenstein, J.L.R. (2022). LiCl treatment leads to long-term restoration of spine maturation and synaptogenesis in adult Tbr1 mutants. J. Neurodev. Disord. *14*, 11.
59. Munz, M., Bharioke, A., Kosche, G., Moreno-Juan, V., Brignall, A., Rodrigues, T.M., Graff-Meyer, A., Ulmer, T., Haeuselmann, S., Pavlinic, D., et al. (2023). Pyramidal neurons form active, transient, multilayered circuits perturbed by autism-associated mutations at the inception of neocortex. Cell *186*, 1930–1949.e31.
60. Mohler, P.J., Schott, J.J., Gramolini, A.O., Dilly, K.W., Guatimosim, S., duBell, W.H., Song, L.S., Haurogné, K., Kyndt, F., Ali, M.E., et al. (2003). Ankyrin-B mutation causes type 4 long-QT cardiac arrhythmia and sudden cardiac death. Nature *421*, 634–639.
61. Brager, D.H., and Johnston, D. (2014). Channelopathies and dendritic dysfunction in fragile X syndrome. Brain Res. Bull. *103*, 11–17.
62. Brandalise, F., Kalmbach, B.E., Cook, E.P., and Brager, D.H. (2023). Impaired dendritic spike generation in the Fragile X prefrontal cortex is due to loss of dendritic sodium channels. J. Physiol. *601*, 831–845.
63. Johnston, D., Frick, A., and Poolos, N.P. (2016). Dendrites and disease. In Dendrites, G. Stuart, N. Spruston, and M. Häusser, eds. (Oxford University Press), pp. 677–702.
64. Nelson, A.D., and Bender, K.J. (2021). Dendritic Integration Dysfunction in Neurodevelopmental Disorders. Dev. Neurosci. *43*, 201–221.
65. Bender, K.J., and Trussell, L.O. (2012). The physiology of the axon initial segment. Annu. Rev. Neurosci. *35*, 249–265.
66. Huang, C.Y., and Rasband, M.N. (2018). Axon initial segments: structure, function, and disease. Ann. N. Y. Acad. Sci. *1420*, 46–61.
67. Kole, M.H., and Stuart, G.J. (2012). Signal processing in the axon initial segment. Neuron *73*, 235–247.
68. Leterrier, C. (2018). The Axon Initial Segment: An Updated Viewpoint. J. Neurosci. *38*, 2135–2145.
69. He, M., Jenkins, P., and Bennett, V. (2012). Cysteine 70 of ankyrin-G is S-palmitoylated and is required for function of ankyrin-G in membrane domain assembly. J. Biol. Chem. *287*, 43995–44005.
70. Globa, A.K., and Bamji, S.X. (2017). Protein palmitoylation in the development and plasticity of neuronal connections. Curr. Opin. Neurobiol. *45*, 210–220.
71. Gupta, J.P., and Jenkins, P.M. (2023). Ankyrin-B is lipid-modified by S-palmitoylation to promote dendritic membrane scaffolding of voltage-gated sodium channel $Na_V1.2$ in neurons. Front. Physiol. *14*, 959660.
72. Chan, W., Kordeli, E., and Bennett, V. (1993). 440-kD ankyrinB: structure of the major developmentally regulated domain and selective localization in unmyelinated axons. J. Cell Biol. *123*, 1463–1473.
73. Kunimoto, M. (1995). A neuron-specific isoform of brain ankyrin, 440-kD ankyrinB, is targeted to the axons of rat cerebellar neurons. J. Cell Biol. *131*, 1821–1829.
74. Kunimoto, M., Otto, E., and Bennett, V. (1991). A new 440-kD isoform is the major ankyrin in neonatal rat brain. J. Cell Biol. *115*, 1319–1331.
75. Popescu, I., Galice, S., Mohler, P.J., and Despa, S. (2016). Elevated local [Ca2+] and CaMKII promote spontaneous Ca2+ release in ankyrin-B-deficient hearts. Cardiovasc. Res. *111*, 287–294.
76. Galante, M., and Marty, A. (2003). Presynaptic ryanodine-sensitive calcium stores contribute to evoked neurotransmitter release at the basket cell-Purkinje cell synapse. J. Neurosci. *23*, 11229–11234.
77. Ramaswamy, S., and Markram, H. (2015). Anatomy and physiology of the thick-tufted layer 5 pyramidal neuron. Front. Cell. Neurosci. *9*, 233.
78. Aru, J., Suzuki, M., and Larkum, M.E. (2020). Cellular Mechanisms of Conscious Processing. Trends Cogn. Sci. *24*, 814–825.
79. Branco, T., Clark, B.A., and Häusser, M. (2010). Dendritic discrimination of temporal input sequences in cortical neurons. Science *329*, 1671–1675.
80. Branco, T., and Häusser, M. (2010). The single dendritic branch as a fundamental functional unit in the nervous system. Curr. Opin. Neurobiol. *20*, 494–502.
81. Gidon, A., Zolnik, T.A., Fidzinski, P., Bolduan, F., Papoutsi, A., Poirazi, P., Holtkamp, M., Vida, I., and Larkum, M.E. (2020). Dendritic action potentials and computation in human layer 2/3 cortical neurons. Science *367*, 83–87.
82. Major, G., Larkum, M.E., and Schiller, J. (2013). Active properties of neocortical pyramidal neuron dendrites. Annu. Rev. Neurosci. *36*, 1–24.
83. Markram, H., Muller, E., Ramaswamy, S., Reimann, M.W., Abdellah, M., Sanchez, C.A., Ailamaki, A., Alonso-Nanclares, L., Antille, N., Arsever, S., et al. (2015). Reconstruction and Simulation of Neocortical Microcircuitry. Cell *163*, 456–492.
84. Smith, S.L., Smith, I.T., Branco, T., and Häusser, M. (2013). Dendritic spikes enhance stimulus selectivity in cortical neurons in vivo. Nature *503*, 115–120.
85. Murayama, M., Pérez-Garci, E., Nevian, T., Bock, T., Senn, W., and Larkum, M.E. (2009). Dendritic encoding of sensory stimuli controlled by deep cortical interneurons. Nature *457*, 1137–1141.
86. Takahashi, N., Ebner, C., Sigl-Glöckner, J., Moberg, S., Nierwetberg, S., and Larkum, M.E. (2020). Active dendritic currents gate descending cortical outputs in perception. Nat. Neurosci. *23*, 1277–1285.
87. Takahashi, N., Oertner, T.G., Hegemann, P., and Larkum, M.E. (2016). Active cortical dendrites modulate perception. Science *354*, 1587–1590.
88. Xu, N.L., Harnett, M.T., Williams, S.R., Huber, D., O'Connor, D.H., Svoboda, K., and Magee, J.C. (2012). Nonlinear dendritic integration of sensory and motor input during an active sensing task. Nature *492*, 247–251.
89. Suzuki, M., and Larkum, M.E. (2020). General Anesthesia Decouples Cortical Pyramidal Neurons. Cell *180*, 666–676.e13.
90. Bock, T., and Stuart, G.J. (2016). The Impact of BK Channels on Cellular Excitability Depends on their Subcellular Location. Front. Cell. Neurosci. *10*, 206.
91. Gonzalez, K.C., Losonczy, A., and Negrean, A. (2022). Dendritic Excitability and Synaptic Plasticity In Vitro and In Vivo. Neuroscience *489*, 165–175.
92. Harnett, M.T., Magee, J.C., and Williams, S.R. (2015). Distribution and function of HCN channels in the apical dendritic tuft of neocortical pyramidal neurons. J. Neurosci. *35*, 1024–1037.
93. Harnett, M.T., Xu, N.L., Magee, J.C., and Williams, S.R. (2013). Potassium channels control the interaction between active dendritic integration compartments in layer 5 cortical pyramidal neurons. Neuron *79*, 516–529.
94. Magee, J.C., and Johnston, D. (1995). Characterization of single voltage-gated Na+ and Ca2+ channels in apical dendrites of rat CA1 pyramidal neurons. J. Physiol. *487*, 67–90.
95. Shah, M.M. (2014). Cortical HCN channels: function, trafficking and plasticity. J. Physiol. *592*, 2711–2719.
96. Gidon, A., and Segev, I. (2012). Principles governing the operation of synaptic inhibition in dendrites. Neuron *75*, 330–341.
97. Megías, M., Emri, Z., Freund, T.F., and Gulyás, A.I. (2001). Total number and distribution of inhibitory and excitatory synapses on hippocampal CA1 pyramidal cells. Neuroscience *102*, 527–540.
98. Ujfalussy, B.B., Makara, J.K., Branco, T., and Lengyel, M. (2015). Dendritic nonlinearities are tuned for efficient spike-based computations in cortical circuits. eLife *4*, e10056.
99. Wilson, N.R., Runyan, C.A., Wang, F.L., and Sur, M. (2012). Division and subtraction by distinct cortical inhibitory networks in vivo. Nature *488*, 343–348.

100. Zhang, D., Li, Y., Rasch, M.J., and Wu, S. (2013). Nonlinear multiplicative dendritic integration in neuron and network models. Front. Comput. Neurosci. *7*, 56.

101. Colasante, G., Lignani, G., Brusco, S., Di Berardino, C., Carpenter, J., Giannelli, S., Valassina, N., Bido, S., Ricci, R., Castoldi, V., et al. (2020). dCas9-Based Scn1a Gene Activation Restores Inhibitory Interneuron Excitability and Attenuates Seizures in Dravet Syndrome Mice. Mol. Ther. *28*, 235–253.

102. Derbis, M., Kul, E., Niewiadomska, D., Sekrecki, M., Piasecka, A., Taylor, K., Hukema, R.K., Stork, O., and Sobczak, K. (2021). Short antisense oligonucleotides alleviate the pleiotropic toxicity of RNA harboring expanded CGG repeats. Nat. Commun. *12*, 1265.

103. Han, Z., Chen, C., Christiansen, A., Ji, S., Lin, Q., Anumonwo, C., Liu, C., Leiser, S.C., Meena, A., Aznarez, I., et al. (2020). Antisense oligonucleotides increase Scn1a expression and reduce seizures and SUDEP incidence in a mouse model of Dravet syndrome. Sci. Transl. Med. *12*, eaaz6100.

104. Ure, K., Lu, H., Wang, W., Ito-Ishida, A., Wu, Z., He, L.J., Sztainberg, Y., Chen, W., Tang, J., and Zoghbi, H.Y. (2016). Restoration of Mecp2 expression in GABAergic neurons is sufficient to rescue multiple disease features in a mouse model of Rett syndrome. eLife *5*, e14198.

105. Weuring, W., Geerligs, J., and Koeleman, B.P.C. (2021). Gene Therapies for Monogenic Autism Spectrum Disorders. Genes (Basel) *12*, 1667.

106. Wolter, J.M., Mao, H., Fragola, G., Simon, J.M., Krantz, J.L., Bazick, H.O., Oztemiz, B., Stein, J.L., and Zylka, M.J. (2020). Cas9 gene therapy for Angelman syndrome traps Ube3a-ATS long non-coding RNA. Nature *587*, 281–284.

107. Ptáček, L.J. (2015). Episodic disorders: channelopathies and beyond. Annu. Rev. Physiol. *77*, 475–479.

108. Mohler, P.J., Splawski, I., Napolitano, C., Bottelli, G., Sharpe, L., Timothy, K., Priori, S.G., Keating, M.T., and Bennett, V. (2004). A cardiac arrhythmia syndrome caused by loss of ankyrin-B function. Proc. Natl. Acad. Sci. USA *101*, 9137–9142.

109. Swayne, L.A., Murphy, N.P., Asuri, S., Chen, L., Xu, X., McIntosh, S., Wang, C., Lancione, P.J., Roberts, J.D., Kerr, C., et al. (2017). Novel Variant in the ANK2 Membrane-Binding Domain Is Associated With Ankyrin-B Syndrome and Structural Heart Disease in a First Nations Population With a High Rate of Long QT Syndrome. Circ. Cardiovasc. Genet. *10*, e001537.

110. Sanders, S.J., Campbell, A.J., Cottrell, J.R., Moller, R.S., Wagner, F.F., Auldridge, A.L., Bernier, R.A., Catterall, W.A., Chung, W.K., Empfield, J.R., et al. (2018). Progress in Understanding and Treating SCN2A-Mediated Disorders. Trends Neurosci. *41*, 442–456.

111. Mishra, V., Karumuri, B.K., Gautier, N.M., Liu, R., Hutson, T.N., Vanhoof-Villalba, S.L., Vlachos, I., Iasemidis, L., and Glasscock, E. (2017). Scn2a deletion improves survival and brain-heart dynamics in the Kcna1-null mouse model of sudden unexpected death in epilepsy (SUDEP). Hum. Mol. Genet. *26*, 2091–2103.

112. Planells-Cases, R., Caprini, M., Zhang, J., Rockenstein, E.M., Rivera, R.R., Murre, C., Masliah, E., and Montal, M. (2000). Neuronal death and perinatal lethality in voltage-gated sodium channel alpha(II)-deficient mice. Biophys. J. *78*, 2878–2891.

113. Bouza, A.A., Edokobi, N., Hodges, S.L., Pinsky, A.M., Offord, J., Piao, L., Zhao, Y.T., Lopatin, A.N., Lopez-Santiago, L.F., and Isom, L.L. (2021). Sodium channel β1 subunits participate in regulated intramembrane proteolysis-excitation coupling. JCI Insight *6*, e141776.

114. Mohler, P.J., Gramolini, A.O., and Bennett, V. (2002). The ankyrin-B C-terminal domain determines activity of ankyrin-B/G chimeras in rescue of abnormal inositol 1,4,5-trisphosphate and ryanodine receptor distribution in ankyrin-B (-/-) neonatal cardiomyocytes. J. Biol. Chem. *277*, 10599–10607.

115. Kizhatil, K., Davis, J.Q., Davis, L., Hoffman, J., Hogan, B.L., and Bennett, V. (2007). Ankyrin-G is a molecular partner of E-cadherin in epithelial cells and early embryos. J. Biol. Chem. *282*, 26552–26561.

116. He, M., Abdi, K.M., and Bennett, V. (2014). Ankyrin-G palmitoylation and βII-spectrin binding to phosphoinositide lipids drive lateral membrane assembly. J. Cell Biol. *206*, 273–288.

117. Ayalon, G., Davis, J.Q., Scotland, P.B., and Bennett, V. (2008). An ankyrin-based mechanism for functional organization of dystrophin and dystroglycan. Cell *135*, 1189–1200.

118. Schindelin, J., Arganda-Carreras, I., Frise, E., Kaynig, V., Longair, M., Pietzsch, T., Preibisch, S., Rueden, C., Saalfeld, S., Schmid, B., et al. (2012). Fiji: an open-source platform for biological-image analysis. Nat. Methods *9*, 676–682.

119. Schamiloglu, S., Lewis, E., Keeshen, C.M., Hergarden, A.C., Bender, K.J., and Whistler, J.L. (2023). Arrestin-3 Agonism at Dopamine D_3 Receptors Defines a Subclass of Second-Generation Antipsychotics That Promotes Drug Tolerance. Biol. Psychiatry *94*, 531–542.

120. Patino, G.A., Claes, L.R., Lopez-Santiago, L.F., Slat, E.A., Dondeti, R.S., Chen, C., O'Malley, H.A., Gray, C.B., Miyazaki, H., Nukina, N., et al. (2009). A functional null mutation of SCN1B in a patient with Dravet syndrome. J. Neurosci. *29*, 10764–10778.

121. Bender, K.J., Ford, C.P., and Trussell, L.O. (2010). Dopaminergic modulation of axon initial segment calcium channels regulates action potential initiation. Neuron *68*, 500–511.

122. Bender, K.J., and Trussell, L.O. (2009). Axon initial segment Ca2+ channels influence action potential generation and timing. Neuron *61*, 259–271.

123. Clarkson, R.L., Liptak, A.T., Gee, S.M., Sohal, V.S., and Bender, K.J. (2017). D3 Receptors Regulate Excitability in a Unique Class of Prefrontal Pyramidal Cells. J. Neurosci. *37*, 5846–5860.

124. Pernía-Andrade, A.J., Goswami, S.P., Stickler, Y., Fröbe, U., Schlögl, A., and Jonas, P. (2012). A deconvolution-based method with high sensitivity and temporal resolution for detection of spontaneous synaptic currents in vitro and in vivo. Biophys. J. *103*, 1429–1439.

125. Tzounopoulos, T., Kim, Y., Oertel, D., and Trussell, L.O. (2004). Cell-specific, spike timing-dependent plasticities in the dorsal cochlear nucleus. Nat. Neurosci. *7*, 719–725.

126. Yasuda, R., Nimchinsky, E.A., Scheuss, V., Pologruto, T.A., Oertner, T.G., Sabatini, B.L., and Svoboda, K. (2004). Imaging calcium concentration dynamics in small neuronal compartments. Sci. STKE *2004*, pl5.

127. Coupé, P., Munz, M., Manjón, J.V., Ruthazer, E.S., and Collins, D.L. (2012). A CANDLE for a deeper in vivo insight. Med. Image Anal. *16*, 849–864.

STAR★METHODS

KEY RESOURCES TABLE

REAGENT or RESOURCE	SOURCE	IDENTIFIER
Antibodies		
Rabbit anti-ankyrin-G C-terminus	Lab-generated	PMID: 17620337
Goat anti-ankyrin-G C-terminus	Lab-generated	PMID: 25049274
Rabbit anti-270/480 kDa ankyrin-G	Lab-generated	PMID: 25552556
Rabbit anti-480 kDa ankyrin-G	Lab-generated	PMID: 25552556
Rabbit anti-ankyrin-B C-terminus	Lab-generated	PMID: 19109891
Sheep anti-ankyrin-B C-terminus	Lab-generated	N/A
Rabbit anti-$Na_V1.2$	Abcam	ab65163
Mouse anti-FLAG M2	Sigma	F3165
Chicken anti-GFP	Abcam	ab13970
mouse anti-HA 6E2	Cell Signaling Technologies	mAb #2367
Rabbit anti-HA	Cell Signaling Technologies	mAb #3724
Guinea pig anti-MAP2	Synaptic Systems	188-004
Bacterial and virus strains		
One Shot Top10 chemically competent *E. Coli*	Thermo Fisher Scientific	C404010
One Shot BL21(DE3)pLysS Chemically Competent *E. coli*	Thermo Fisher Scientific	C606010
AAV-EF1α-Cre-mCherry	UNC Viral Core	N/A
Chemicals, peptides, and recombinant proteins		
NBQX disodium salt	Tocris	0373
Tetrodotoxin-citrate	Alomone	T-550
(R)-CPP	Tocris	0247
Picrotoxin	Tocris	1128
Fluo-5F, Pentapotassium Salt, cell impermeant	Invitrogen	F14221
Alexa Fluor 594 hydrazide	Invitrogen	A10438
Prolong Gold Antifade Reagent	Invitrogen	P36930
ING-2 TMA^+ Salt	ION Biosciences	2013C
TTA-P2	Alomone	T155
Nifedipine	Tocris	1075
ω-conotoxin-MVIIC	Vivitide	PCN-4283-s
Ro 25-6981	Tocris	1594
Critical commercial assays		
Duolink proximity ligation assay	Sigma-Aldrich	DUO92101
Experimental models: Cell lines		
HEK293 cells	American Type Culture Collection	CRL-1573
Experimental models: Organisms/strains		
Mouse: C57BL/6J	The Jackson Laboratory	JAX Strain #:000664 RRID:IMSR_JAX:000664
Mouse: *Ank2* exon 24 flox: B6.129(Cg)-Ank2tm1.1Pmoh/MnrJ	P. Mohler	JAX Strain #031428
Mouse: *Scn2a*$^{+/-}$	M. Montal/E. Glasscock	PMID: 10827969, 28334922
Mouse: Rbp4-Cre-Ai14	J. Rubenstein	PMID: 32294447
Recombinant DNA		
$Na_V1.2$ IRES GFP	Genscript	PMID: 31230762

(*Continued on next page*)

Continued

REAGENT or RESOURCE	SOURCE	IDENTIFIER
$Na_V1.2$-3xFLAG IRES GFP	This study	N/A
Δ9 $Na_V1.2$-3xFLAG IRES GFP	This study	N/A
220 kDa ankyrin-B-GFP	V. Bennett	PMID: 11781319
220 kDa ankyrin-B F131Q/F164Q	This study	N/A
440 kDa ankyrin-B-Halo tag	V. Bennett	PMID: 31285321
440 kDa ankyrin-B-GFP	This study	N/A
pENTR-D-TOPO	Invitrogen	K240020
Na_V β1-V5-2A-DsRed	L. Isom	PMID: 33411695
Δ9 $Na_V1.2$ II-III loop-3xHA	This study	N/A
pCSF107mT-GATEWAY-3'-3HA	Addgene	Addgene plasmid # 67616
TagBFP-N	Evrogen	#FP172
Cre-2A-TagBFP	V. Bennett	PMID: 25552561
Software and algorithms		
Fiji	http://fiji.sc	RRID:SCR_002285
pClamp	Molecular Devices	RRID:SCR_011323; v10
IGOR Pro	Wavemetrics	RRID:SCR_000325; v6.3
Prism	Graphpad	RRID:SCR_002798; v9
IMARIS	Bitplane	RRID:SCR_007370; v9.9
Pyramidal cell compartment model	NEURON environment (v7.7) based on the Blue Brain Project thick-tufted layer 5b pyramidal cell (TTPC1) model	PMID: 28256214
Postsynaptic current event detection code	benderlab.ucsf.edu/resources	PMID: 23062335

RESOURCE AVAILABILITY

Lead contact

Further information and requests for resources and reagents should be directed to and will be fulfilled by the lead contact, Paul Jenkins (pjenkins@umich.edu).

Materials availability

Plasmids generated in this study are available from the lead contact upon request.

Data and code availability

Data reported in this paper are available from the lead contact upon reasonable request. This paper does not report original code. Any additional information required to reanalyze the data reported in this paper is available from the lead contact upon request.

EXPERIMENTAL MODEL AND STUDY PARTICIPANT DETAILS

Mouse strains

All experimental procedures were performed in accordance with UCSF and UM IACUC guidelines. All experiments were performed on mice housed under standard conditions with *ad libitum* access to food and water, with colonies maintained in-house. C57BL/6J mice were obtained from Jackson Laboratories (stock #000664). The *Ank2* exon $24^{flox/flox}$ mouse line was a gift from Dr. Peter Mohler (The Ohio State University).[31] *Scn2a*$^{+/-}$ mice were provided by Drs. E. Glasscock and M. Montal.[111,112] Rbp4-Cre-Ai14 (Gensat K100) mice were kindly provided by Dr. John Rubenstein (University of California, San Francisco).[58]

METHOD DETAILS

Constructs, antibodies, and experimental models

Human $Na_V1.2$-3xFLAG IRES eGFP was generated by Genscript (Piscataway, NJ) by the addition of a short linker (AAARG) and a triple-FLAG epitope (DYKDHDGDYKDHDIDYKDDDDK) to the carboxyl terminus of codon-optimized human $Na_V1.2$ IRES eGFP.[7] Δ9 $Na_V1.2$-3xFLAG IRES eGFP was created by Genscript by deletion of the necessary nine amino acid core ankyrin-binding motif, described previously.[12] The HA-tagged $Na_V1.2$ II-III loops (wild-type and Δ9) were created by cloning the coding sequence corresponding to amino acids 991-1211 of human $Na_V1.2$ into pENTR D-TOPO by polymerase chain reaction. The loops were shuttled

into pCSF107mT-GATEWAY-3'-3HA (gift from Todd Stukenberg, Addgene plasmid # 67616) using Gateway LR clonase, according to manufacturer's directions (Thermo Fisher). Na_V β1-V5-2A-DsRed was a generous gift from Dr. Lori Isom (University of Michigan).[113] 220 kDa ankyrin-B-GFP was previously described.[114] 440 kDa ankyrin-B-GFP was created by subcloning the additional giant exon from 440 kDa ankyrin-B-Halo[38] into 220 kDa ankyrin-B-GFP using BstZ17I and SacII sites. 220 kDa ankyrin-B F131Q/F164Q[33] was created by Genscript by site-directed mutagenesis. TagBFP and Cre-2A-TagBFP were previously described.[41] All plasmids were sequenced across the entire coding sequence by Sanger sequencing prior to use in experiments.

Lab-generated antibodies to ankyrin-B and ankyrin-G were described previously, including rabbit anti-ankyrin-G C-terminus,[115] goat anti-ankyrin-G C-terminus,[116] rabbit anti-270/480 kDa ankyrin-G,[14] rabbit anti-480kDa ankyrin-G,[14] rabbit anti-ankyrin-B C-terminus,[117] sheep anti-ankyrin-B C-terminus. Specificity of all lab-generated antibodies are confirmed using respective null mouse tissue. In addition, antibodies are tested for ankyrin cross-reactivity by both immunocytochemistry and western blotting in HEK293 cells expressing 220 kDa ankyrin-B-GFP or 190 kDa ankyrin-G-GFP. Commercial antibodies used in these studies include rabbit anti-Nav1.2 (Abcam, ab65163), mouse anti-FLAG-M2 (Sigma, F3165), chicken anti-GFP (Abcam, ab13970), mouse anti-HA epitope (clone 6E2, Cell Signaling Technologies), rabbit anti-HA epitope (clone C29F4, Cell Signaling Technologies), and guinea pig anti-MAP2 (Synaptic Systems, 188-004).

Co-immunoprecipitation

Whole brain was dissected from C57Bl/6J adult mice (P60-75). Each brain was homogenized in 2 ml of reaction buffer (0.3 M sucrose, 10 mM Phosphate, 2 mM EDTA; pH 7.4), mixed with phosphatase inhibitor and protease inhibitor. 500 μL of 20 mM DSP (Lomant's Reagent) was added to the sample and incubated for 2 hours on ice, after which the crosslinking reaction was quenched by adding 1x Tris to a final concentration of 50 mM and incubated on ice for 15 minutes. Samples were lysed by mixing with lysis buffer (30 mM Tris, 150 mM NaCl, 2 mM EDTA, 1% IGEPAL, 0.5% Sodium Deoxycholate; pH 6.8) and sonicating 20 times at 1-second-long pulses, followed by ultracentrifugation at 100k x g for 30 minutes. Solubilized proteins were then subjected to immunoprecipitation using magnetic beads bound to antibodies (Bio-Rad SureBeads Protein A; rabbit ankyrin-B 1:250, rabbit Nav1.2 1:100, rabbit IgG 1:250). Lysate samples were rotated with the bead mixture overnight at 4°C. Beads were collected the next day, washed 3 times with lysis buffer, and mixed 1:1 with 5x PAGE buffer (5% SDS, 25% sucrose, 50 mM Tris; pH 9, 0,5 mM EDTA) and heated to 68°C for 10 minutes.

Western blot

Samples were separated on a 3.5-17% gradient gel in 1x Tris buffer, pH 7.4 (40 mM Tris, 20 mM NaOAc, and 2mM NaEDTA) with 0.2% SDS. Transfer to nitrocellulose membrane was performed overnight at 300 mA at 4°C in 0.5x Tris buffer with 0.01% SDS. Membranes were blocked with 5% Bovine Serum Albumin (BSA) in TBS at room temperature for 1 hour and incubated in primary antibodies (rabbit ankyrin-B 1:1000; rabbit ankyrin-G 1:1000; rabbit Nav1.2 1:500; mouse α-tubulin 1:1000) diluted in 5% BSA in TBS-T overnight at 4°C. Membranes were washed 3x for 10 minutes with TBS-T and incubated for 1 hr at room temperature with LiCor fluorescent secondaries (1:15,000) in 5% BSA in TBS-T. Membranes were then washed 3x for 10 minutes in TBS-T, 3x for 5 minutes in ddH_2O) before being imaged on LiCor Odyssey Clx imager.

Proximity ligation assay

HEK293 cells were obtained from the American Type Culture Collection and maintained in a humidified environment at 37 °C with 5% CO_2. Cells were cultured in DMEM (Invitrogen #11995) with 10% fetal bovine serum, 100 units/ml penicillin, and 100 units/ml streptomycin. 100,000 cells were plated onto glass-bottomed dishes (Cellvis) and were allowed to attach for four hours. Cells were transfected with 100 ng of each plasmid ($Na_V1.2$ II-III loop-3xHA and 220 kDa ankyrin-B-GFP) with Lipofectamine 2000, according to the manufacturer's protocol. After 16 hours, cells were fixed with 4% paraformaldehyde for 15 minutes, permeabilized with 0.1% Triton X-100 for 10 minutes and blocked with 5% bovine serum albumin and 0.2% Tween-20 in PBS for 30 minutes. Cells were incubated with primary antibodies (mouse anti-HA and rabbit anti-ankyrin-B C terminus) in blocking buffer overnight in a humidified chamber. The next day, cells were washed with PBS containing 0.2% Tween-20 (PBS-T) three times for 10 minutes and incubated with anti-mouse minus and anti-rabbit plus PLA probes. Samples were processed for ligation amplification using red fluorescent nucleotides, and mounting, according to the manufacturer's protocol (Duolink, Sigma-Aldrich).

Neocortical cultures, transfections, and immunofluorescence

Primary neocortex was dissected from postnatal day 0 (P0) mice and treated with 0.25% trypsin and 100 μg/ml DNase I in 2 mL HBSS with 10mM HEPES, then triturated gently through a glass pipette with a fire-polished tip. The dissociated neurons were then plated on 35mm MatTek dishes, precoated with poly-D-lysine and laminin, in 0.5mL of Neurobasal-A medium containing 10% FBS, B27 supplement, 2 mM glutamine, and penicillin/streptomycin. On day *in vitro* 1 (DIV1), the neurons were washed with Neurobasal-A medium and fed with growth media (2.5mL of fresh Neurobasal-A medium containing 1% FBS, B27, glutamine, penicillin/streptomycin, and 2.5 μg/ml AraC. On DIV3, plasmids were introduced into neocortical neurons through lipofectamine 2000-mediated transfection. In one tube, 500 ng of each plasmid was added to 200 μL of Neurobasal-A, and in a second tube, lipofectamine 2000 (3 μL/ 1 μg plasmid) was added to 200 μL of Neurobasal-A. The two tubes were then mixed and incubated at room temperature for 15 min. The neuronal growth media was then removed from the dishes and saved, and transfection media was added to the neurons. Cells

were incubated in transfection media for 1 hr at 37°C. The transfection media was aspirated, cells were washed once with warm Neurobasal-A, and growth media was added back to plates. The cells were maintained in culture until 7 DIV or 21 DIV and fixed for immunofluorescence as described below.

Dissociated neocortical neurons were fixed for 15 minutes at room temperature with 4% paraformaldehyde, followed by permeabilization with 0.2% Triton in 1X PBS pH7.4 for 10 minutes at room temperature. They were then blocked with blocking buffer (5% BSA, 0.2% Tween 20 in 1X PBS pH7.4) at room temperature for 30 minutes. Primary antibodies were diluted in blocking buffer and incubated overnight at 4 °C. The next day, cells were washed at room temperature three times for 15 minutes with PBS containing 0.2% Tween 20. Then the cells were incubated with secondary antibodies diluted in blocking buffer for one hour at room temperature. The cells were washed at room temperature three times for 15 minutes with PBS containing 0.2% Tween 20 and then mounted with ProLong Gold antifade reagent before imaging with confocal microscopy as described below.

Confocal microscopy

Samples were imaged on a Zeiss LSM 880 with Airyscan using a 63× 1.4 Plan-Apochromat objective and excitation was accomplished using 405-, 488-, 561-, and 633-nm lasers. Each experiment was repeated at least three independent times. Measurements were taken using Fiji software.[118] Laser power and imaging parameters were kept constant for each immunocytochemistry condition. Line profiles (Figure 4H) were calculated as described previously.[119]

In vitro cell electrophysiology

Voltage-clamp recordings were performed at room temperature in standard whole-cell configuration, using Axopatch 700B amplifier and pClamp (version 10, Axon Instruments, FosterCity, CA) and a Digidata 1440A digitizer (Molecular Devices). Sodium current was recorded in the presence of external recording solution containing in mM: 120 NaCl, 4 KCl, 1 $MgCl_2$, 1.5 $CaCl_2$, 10 HEPES, 45 Glucose and 30 Sucrose (pH 7.35 with CsOH; osmolality was 300–305 mOsm). For the β1 subunit co-transfection experiments, the external sodium concentration was reduced to 60mM. Fire-polished patch pipettes obtained from borosilicate glass capillary (WPI) which resistance was between 1.5-3.5 MΩ, were filled with an internal solution containing in mM: 10 NaCl, 105 Cs-Aspartate, 10 CsCl, 10 EGTA, 10 HEPES, (pH 7.2 with H_2SO_4). To determine sodium current amplitude and voltage dependence of activation, currents were evoked by depolarization for 250 ms to different potentials (from −120 to 30 mV on 5 or 10 mV steps) from holding potential of −80 mV and a hyperpolarizing −120mV, 250 ms pre-pulse. Voltage-dependence of inactivation was determined by applying a 50 ms test pulse of 0 mV after the 250 ms pulses used for voltage dependence of activation. Series resistance was compensated no more than 40%–65% when needed, and leak subtraction was performed by application of a standard P/4 protocol. Signals were low-pass filtered at 10 kHz, and data were sampled at 40 kHz online. Current densities were determined by dividing current amplitude by the cell capacitance (Cm) measured by pClamp software. Normalized conductance and inactivation curves were generated as previously described.[120]

Compartmental modeling

A pyramidal cell compartmental model was implemented in the NEURON environment (v7.7) based on the Blue Brain Project thick-tufted layer 5b pyramidal cell (TTPC1) model used in our previous study.[7,26,77,83] The TTPC1 model was adjusted to include an AIS, and the original Na channels in the TTPC1 model were replaced with $Na_V1.2$ and $Na_V1.6$ channels in compartments with densities as previously shown.[26] For phase plane comparisons, the first AP was evoked with a stimulus of 500 pA intensity (25 ms duration) in each model configuration. Threshold was defined as the membrane potential when dV/dt exceeds 15 V/s. For AP backpropagation, a single AP was evoked with a 1.2 nA, 8 ms step current applied to the somatic membrane. In model conditions with only $Na_V1.2$ contributing Na conductance in the distal apical dendrite, $Na_V1.6$ was replaced with $Na_V1.2$ after ~30 microns from soma and total $Na_V1.2$ conductance was increased by a factor of 1.9 to match total conductance levels in the mixed $Na_V1.2$/$Na_V1.6$ model (since $Na_V1.6$ voltage dependence is more hyperpolarized). Voltage was recorded from the soma, shaft of the apical dendrite (460 μm from soma), and branch of the apical tuft (975 μm from soma). Conductance densities for sodium channels in different compartments across models were as in Table S1.

Ex vivo electrophysiology

Mice aged P55-75 were anesthetized under isoflurane. Brains were dissected and placed in 4 °C cutting solution consisting of (in mM) 87 NaCl, 25 $NaHCO_3$, 25 glucose, 75 sucrose, 2.5 KCl, 1.25 NaH_2PO_4, 0.5 $CaCl_2$, and 7 $MgCl_2$ and bubbled with 5% CO_2/95% O_2. Coronal slices 250 μm-thick were obtained that included the medial prefrontal cortex. Slices were then incubated in a holding chamber with sucrose solution for 30 mins at 33 °C, then placed at room temperature until recording. Recording solution consisted of (in mM): 125 NaCl, 2.5 KCl, 2 $CaCl_2$, 1 $MgCl_2$, 25 $NaHCO_3$, 1.25 NaH_2PO_4, 25 glucose, bubbled with 5% CO_2/95% O_2. Osmolarity of the recording solution was adjusted to approximately 310 mOsm. All recordings were performed at 32-34 °C.

Neurons were identified using differential interference contrast (DIC) optics for conventional visually-guided whole-cell recording, or with two-photon-guided imaging of AAV-EF1α-Cre-mCherry fluorescence overlaid on a scanning DIC image of the slice. Patch electrodes were pulled from Schott 8250 glass (3-4 MΩ tip resistance). For current-clamp recordings, patch electrodes were filled with a K-gluconate-based internal solution that contained (in mM): 113 K-Gluconate, 9 HEPES, 4.5 $MgCl_2$, 0.1 EGTA, 14 $Tris_2$-phosphocreatine, 4 Na_2-ATP, 0.3 Tris-GTP; 290 mOSM, pH: 7.2-7.25. For Ca^{2+} imaging, EGTA was replaced with 250 μM Fluo-5F and

20 μM Alexa 594. For voltage-clamp recordings, a CsCl-based internal solution was used that contained (in mM): 110 $CsMeSO_3$, 40 HEPES, 1 KCl, 4 NaCl, 4 Mg-ATP, 10 Na-phosphocreatine, 0.4 Na_2-GTP, 5 QX-314, and 0.1 EGTA; ~290 mOsm, pH 7.22.

Electrophysiological recordings were collected with a Multiclamp 700B amplifier (Molecular Devices) and a custom data acquisition program in Igor Pro software (Wavemetrics). Current-clamp recordings of action potential waveform were acquired at 50 kHz and filtered at 20 kHz. Pipette capacitance was compensated by 50% of the fast capacitance measure under gigaohm seal conditions in voltage-clamp prior to establishing a whole-cell configuration, and the bridge was balanced. Voltage-clamp experiments were acquired at 10-20 kHz and filtered at 3-10 kHz. Pipette capacitance was completely compensated, and series resistance was compensated 50%. All data were corrected for measured junction potentials of 12 and 11 mV in K-gluconate and Cs-based internals, respectively. Data inclusion was based on previously established metrics,[9,121,122] and includes measures for recording stability and cell health [e.g., stable series resistance of <18 MΩ, stable membrane potential (V_m), and input resistance (R_{in}), with less than 15% change over data collection epochs]. All recordings were made using a quartz electrode holder (Sutter Instrument) to minimize electrode drift within the slice.

All acute slice recordings were made from layer 5b thick-tufted pyramidal tract (PT) neurons in the medial prefrontal cortex. In current-clamp, layer 5b neurons were characterized as those that exhibited a voltage rebound more depolarizing that V_{rest} in response to a strong hyperpolarizing current (-400 pA, 120 ms) that peaked within 90 ms of current offset and depolarizing (300 ms, 20-300 pA) square current pulses from a holding potential of -80 mV.[123] AP threshold, AIS dV/dt and peak dV/dt measurements were determined from the first AP evoked by a step current (300 ms duration; 200-300 pA) delivered to the somatic pipette within the first 2 minutes of establishing the whole-cell recording configuration. AP threshold was defined as the V_m when dV/dt first exceeded 15 V/s. AIS peak dV/dt was defined at the saddle point between two positive inflection points in the second voltage derivative that occur during the depolarizing phase of the AP.

Miniature excitatory and inhibitory postsynaptic currents (mEPSCs, mIPSCs) were acquired in voltage-clamp configuration at -80 mV and 0 mV, respectively, in the presence of 10 μM R-CPP and 400 nM TTX. Events were analyzed using a deconvolution-based event detection algorithm within IgorPro.[124] Detectable events were identified using a noise threshold of 3.5x with a minimum amplitude of 2 pA and a 2 ms inter-event interval. Events were subsequently manually screened to confirm appropriate event detection. Event detection code is available at benderlab.ucsf.edu/resources. Cumulative probability distribution of mEPSCs and mIPSCs event intervals were generated per cell and then averaged. Distributions were compared using the Kolmogorov-Smirnov test. A confidence interval of 95% ($P < 0.05$) was required for values to be considered statistically significant. In experiments measuring AMPA:NMDA ratio and paired-pulse ratio (PPR), EPSCs were evoked using a bipolar glass theta electrode placed in layer 5b ~200 μm lateral from the recording neuron. AMPA: NMDA ratio was initially measured at -80 mV to assess the AMPA contribution and then at +30 mV to evaluate the NMDA-mediated component in the presence of 25 μM picrotoxin. AMPA was defined as the peak inward current at -80 mV and NMDA as the outward current 50 ms after stimulus onset at +30 mV. PPR was acquired at -80 mV in the presence of 10 μM R-CPP and 25 μM picrotoxin. For Ro 25-6981 (Tocris cat. # 1594) experiments, external aCSF also included 10 μM NBQX and 25 μM picrotoxin to block AMPA-receptors and $GABA_A$-receptors, respectively. Evoked NMDAR-mediated EPSCs were recorded at +30 mV before and 40-45 min after Ro 26-6981 (1 μM) application. EPSC decay was fitted with a double exponential and the normalized weighted time constant was calculated on a cell-by-cell basis.

mEPSCs, mIPSCs, and AMPA:NMDA ratio were collected from *Ank2*$^{+/fl}$ mice injected with AAV-EF1α-Cre-mCherry and WT littermates. Mice were anesthetized with isofluorane and positioned in a stereotaxic apparatus. 500 nL volumes of AAV-EF1α-Cre-mCherry (UNC vector core) were injected into the mPFC of *Ank2*$^{+/fl}$ mice (stereotaxic coordinates [mm]: anterior-posterior [AP] +1.7; mediolateral [ML] -0.35; dorsoventral [DV]: -2.6). Experiments were conducted four-week post-injection. Paired-pulse ratio (PPR) was recorded from *Ank2*$^{+/fl}$::CaMKIIα-Cre mice and WT littermates. For AMPA:NMDA and PPR experiments in spare Cre-expressing animals, AAV-EF1α-Cre-mCherry was diluted 1:3 in saline, then injected into the mPFC of *Ank2*$^{+/fl}$ mice. To generate synaptic input-output (I/O) curves, EPSPs were isolated with 25 μM picrotoxin and evoked via a glass bipolar electrode placed ~50 μm lateral from somatic recording pipette in layer 5. Threshold was defined as the voltage (200 μs duration) required to evoke an EPSP on at least 8/10 trials (10 sec inter-trial interval) and less than 3/10 trials at 0.9x threshold intensity. Stimulus intensity was then increased in intervals of 1.5x, 2x, 3x, 4x and 5x.

Spike timing-dependent plasticity experiments (STDP) were conducted in *Ank2*$^{+/fl}$::Rbp4-Cre-Ai14 mice to induce *Ank2* haploinsufficiency specifically in layer 5 cortical projection neurons during early embryonic development (E13.5).[58,59] STDP was induced using an established pairing protocol, as in Spratt et al.[9] and Tzounopoulos et al.[125] with EPSPs generated via a stimulating electrode placed 25-50 μm from the layer 1- layer 2/3 border, 300 μm dorsal to a line running perpendicular to the midline pia from the whole-cell pipette. Pairing was induced within 5.5 min of establishing whole-cell recordings.

Two-photon imaging

Two-photon laser scanning microscopy (2PLSM) was performed as previously described.[122] A Coherent Ultra II was tuned to 810 nm for calcium imaging, ING-2 sodium imaging, and morphology experiments. Epi- and transfluorescence signals were captured either through a 40x, 0.8 NA objective for calcium imaging or a 60X, 1.0 NA objective for ING-2 imaging paired with a 1.4 NA oil immersion condenser (Olympus). For calcium imaging, fluorescence was split into red and green channels using dichroic mirrors and band-pass filters (575 DCXR, ET525/70 m-2p, ET620/60 m-2p, Chroma). Green fluorescence (Fluo-5F) was captured with 10770-40 photomultiplier tubes selected for high quantum efficiency and low dark counts (PMTs, Hamamatsu). Red fluorescence (Alexa 594) was

captured with R9110 PMTs. Data were collected in linescan mode (2–2.4 $\Delta(G/R)/(G/R)_{max}$*100, where $(G/R)_{max}$ was the maximal fluorescence in saturating Ca^{2+} (2 mM).[126] AP backpropagation experiments were performed in 25 μM picrotoxin, 10 μM NBQX and 10μM R-CPP. For ING-2 sodium imaging, the epifluorescence filters were removed and the transfluorescence filters were replaced with a single 535/150 bandpass filter (Semrock) and all fluorescence was collected on HA10770-40 PMTs. For ING-2 imaging in the presence of Ca_V blockers, TTA-P2 (2 μM; Alomone Labs cat. #T-155), Nifedipine (10 μM; Tocris cat. # 1075), and ω-conotoxin-MVIIC (1 μM; Vivitide cat. # PCN-4283-s) were applied to 10 mLs aCSF along with 0.001% bovine serum albumin to minimize peptide preabsorption. All calcium channel antagonists stock solutions were prepared in glass vials, and glass tubing and a glass syringe were used for recirculation. Dendritic spine morphology and density images were obtained using 2PLSM at 2x the Nyquist resolution limit at 810 nm excitation, with z-stacks through distal apical dendritic tuft branches (0.2 μm steps in the z-axis) through a 60X, 1.0 NA objective. Stacks were processed post-hoc with the ImageJ CANDLE denoising protocol,[127] then reconstructed using IMARIS v9.9 (Bitplane). Maximum intensity image projections are displayed using the ''Red Hot'' lookup table in FIJI. Full neuronal and dendritic reconstructions were stitched together using pairwise stitching in FIJI before generation of maximum intensity projections.

QUANTIFICATION AND STATISTICAL ANALYSIS

Statistical analysis was performed and presented using Graphpad Prism 9 software. Data were acquired from both sexes and no sex-dependent differences were found. All data were analyzed blind to genotype. Unless otherwise noted, data are presented with box plots (medians and quartiles, with min/max tails) and individual data points overlaid. Data were quantified as mean ± standard error in figure legends and statistical tests were noted. Each data point (n) is indicative of individual neurons. Mean values per cell were compared using the Mann-Whitney test for two groups or Holm-Šídák multiple comparisons test was used to compare three or more groups unless otherwise noted. Results were considered significant at alpha value of $p < 0.05$. ''n.s.'' indicates not significant. Group sample sizes were chosen based on standards in the field and prior, similar experiments conducted by our groups.

Neuron, Volume *112*

Supplemental information

Physical and functional convergence of the autism risk genes *Scn2a* and *Ank2* in neocortical pyramidal cell dendrites

Andrew D. Nelson, Amanda M. Catalfio, Julie P. Gupta, Lia Min, René N. Caballero-Florán, Kendall P. Dean, Carina C. Elvira, Kimberly D. Derderian, Henry Kyoung, Atehsa Sahagun, Stephan J. Sanders, Kevin J. Bender, and Paul M. Jenkins

Supplemental Information

Physical and functional convergence of the autism risk genes *Scn2a* and *Ank2* in neocortical pyramidal cell dendrites

Andrew D. Nelson, Amanda M. Catalfio, Julie P. Gupta, Lia Min, Rene N. Caballero-Floran, Kendall P. Dean, Carina C. Elvira, Kimberly D. Derderian, Henry Kyoung, Atehsa Sahagun, Stephan J. Sanders, Kevin J. Bender*, Paul M. Jenkins*

Figures S1-S9, Table S1.

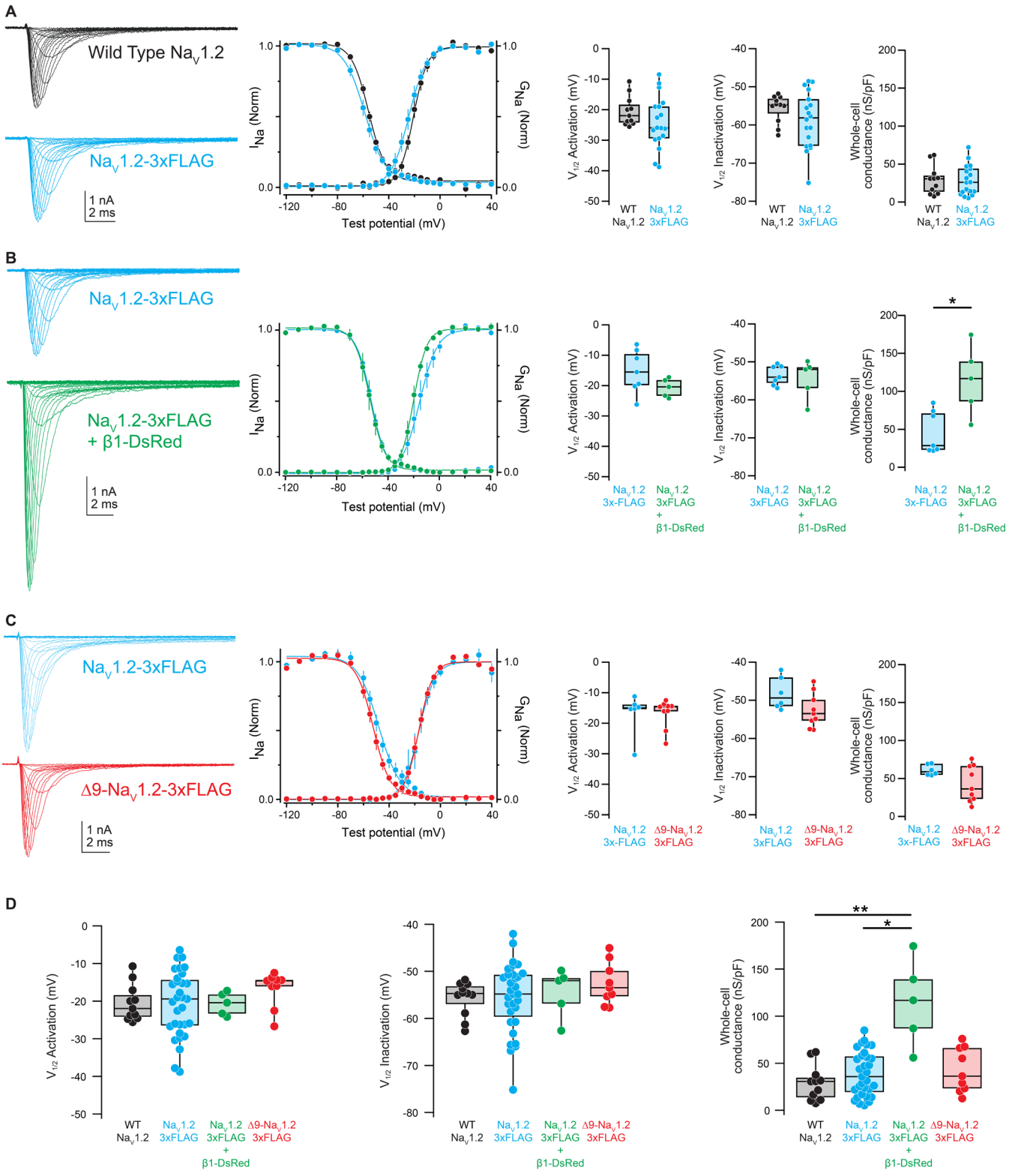

Figure S1: Electrophysiological assays of HEK293 cells transfected with Na$_V$1.2-IRES-eGFP constructs, related to Figures 1-3

(A) Representative currents (left) and activation and inactivation curves (middle) from HEK293 cells transfected with WT Na$_V$1.2 (black) or Na$_V$1.2-3xFLAG-IRES-eGFP (blue). Right: Activation (left)- (WT Na$_V$1.2: -20.5 ± 1.5 mV, n = 11 cells; Na$_V$1.2-3xFLAG: -24.1 ± 2.0 mV, n = 18 cells) p = 0.15. Mann-Whitney test. Inactivation (middle)- (WT Na$_V$1.2: -55.7 ± 1.1 mV, n = 11; Na$_V$1.2-3xFLAG: -58.8 ± 1.7 mV, n = 18) p = 0.26. Mann-Whitney test. Whole cell conductance (right) – (WT Na$_V$1.2: 29.1 ± 5.6 nS/pF, n = 11; Na$_V$1.2-3xFLAG: 28.8 ± 4.6 nS/pF, n = 18) p = 0.95. Mann-Whitney test.

(B) Representative currents (left) and activation and inactivation curves (middle) from HEK293 cells transfected with Na$_V$1.2-3xFLAG-IRES-eGFP (blue) or Na$_V$1.2-3xFLAG-IRES-eGFP plus β1-DsRed (green). Right: Activation (left)- (Na$_V$1.2-3xFLAG: -15.3 ± 2.7 mV, n = 7 cells; Na$_V$1.2-3xFLAG + β1-DsRed: -20.7 ± 3.0 mV, n = 5 cells) p = 0.20. Mann-Whitney test. Inactivation (middle)- (Na$_V$1.2-3xFLAG: -53.5 ± 1.0 mV, n = 7; Na$_V$1.2-3xFLAG + β1-DsRed: -54.5 ± 2.3 mV, n = 5) p = 0.88 Mann-Whitney test. Whole cell

conductance (right) – ($Na_V1.2$-3xFLAG: 46.2 ± 10.6 nS/pF, *n* = 7; $Na_V1.2$-3xFLAG + β1-DsRed: 114.7 ± 20.5 nS/pF, n = 5) *p = 0.018. Mann-Whitney test.

(C) Representative currents (left) and activation and inactivation curves (right) from HEK293 cells transfected with $Na_V1.2$-3xFLAG-IRES-eGFP (blue) or Δ9-$Na_V1.2$-3xFLAG-IRES-eGFP (red). Activation (left)- ($Na_V1.2$-3xFLAG: -16.8 ± 2.8 mV, n = 6 cells; Δ9-$Na_V1.2$-3xFLAG: -16.8 ± 1.6 mV, n = 9 cells) p = 0.95. Mann-Whitney test. Inactivation (middle)- ($Na_V1.2$-3xFLAG: -48.1 ± 1.7 mV, n = 6; Δ9-$Na_V1.2$-3xFLAG: -52.6 ± 1.5 mV, n = 9) p = 0.09. Mann-Whitney test. Whole cell conductance (right) – ($Na_V1.2$-3xFLAG: 39.5 ± 6.9 nS/pF, n = 6; Δ9-$Na_V1.2$-3xFLAG: 43.0 ± 7.9 nS/pF, n = 9) p = 0.65. Mann-Whitney test.

(D) Summary data from panels A-C. Activation (left)- (WT $Na_V1.2$: -20.5 ± 1.5 mV, n = 11 cells; $Na_V1.2$-3xFLAG: -20.7 ± 1.6 mV, n = 31 cells; $Na_V1.2$-3xFLAG + β1-DsRed: -20.7 ± 3.0 mV, n = 5 cells; Δ9-$Na_V1.2$-3xFLAG: -16.8 ± 1.6 mV, n = 9 cells) p = 0.46. Kruskal-Wallis test. Inactivation (middle)- (WT $Na_V1.2$: -55.7 ± 1.1 mV, n = 11; $Na_V1.2$-3xFLAG: -55.5 ± 1.3 mV, n = 31, $Na_V1.2$-3xFLAG + β1-DsRed: -54.5 ± 2.3 mV, n = 5; Δ9-$Na_V1.2$-3xFLAG: -52.6 ± 1.5 mV, n = 9) p =0.67. Kruskal-Wallis test. Whole cell conductance (right) – (WT $Na_V1.2$: 29.1 ± 5.6 nS/pF, n = 11; $Na_V1.2$-3xFLAG: 39.0 ± 4.2 nS/pF, n = 31; $Na_V1.2$-3xFLAG + β1-DsRed: 114.7 ± 20.5 nS/pF, n = 5; Δ9-$Na_V1.2$-3xFLAG: 43.0 ± 7.9 nS/pF, n = 9) p = 0.0065. Kruskal-Wallis test. Dunn's Multiple comparisons: *p=0.01 $Na_V1.2$-3xFLAG vs $Na_V1.2$-3xFLAG + β1-DsRed. ** p=0.004 $Na_V1.2$-IRES-GFP vs $Na_V1.2$-3xFLAG + β1-DsRed.

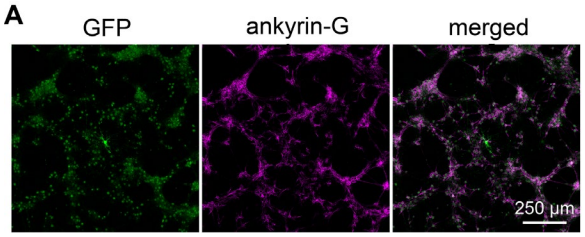

Figure S2: Sparse transient transfection to isolate postsynaptic aspects of ankyrin-B function. Related to Fig. 1-4.

(A) Representative 10x image of a field of a DIV21 cultured neocortical neurons showing a single neuron expressing ankB-GFP stained with GFP (green) and ankyrin-G (magenta).

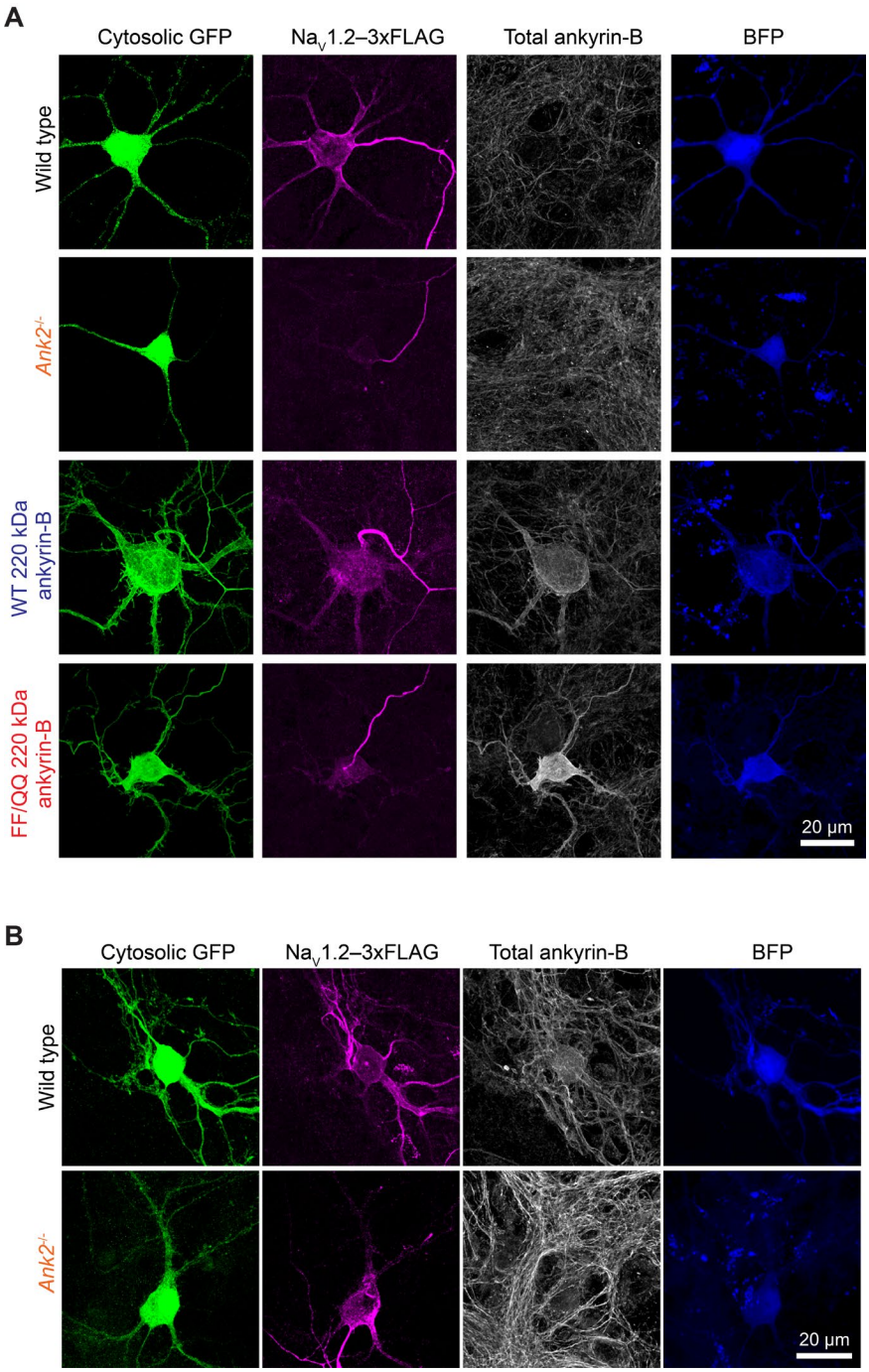

Figure S3: Whole-cell maximum projection images of *Ank2* knockout experiments. Related to Figs 2, 4.

(A) Maximum projection confocal images of neurons in Figure 2A. DIV21 WT or total *Ank2*-null cultured neocortical neurons co-transfected with $Na_V1.2$-3xFLAG-IRES-eGFP and Cre-2A-BFP. Cells were immunostained with antibodies against ankyrin-B (white), FLAG (magenta), GFP (green), or BFP (blue).

(B) Maximum projection confocal images of neurons in Figure 4H. Cells were immunostained with antibodies against ankyrin-B (white), FLAG (magenta), GFP (green), or BFP (blue).

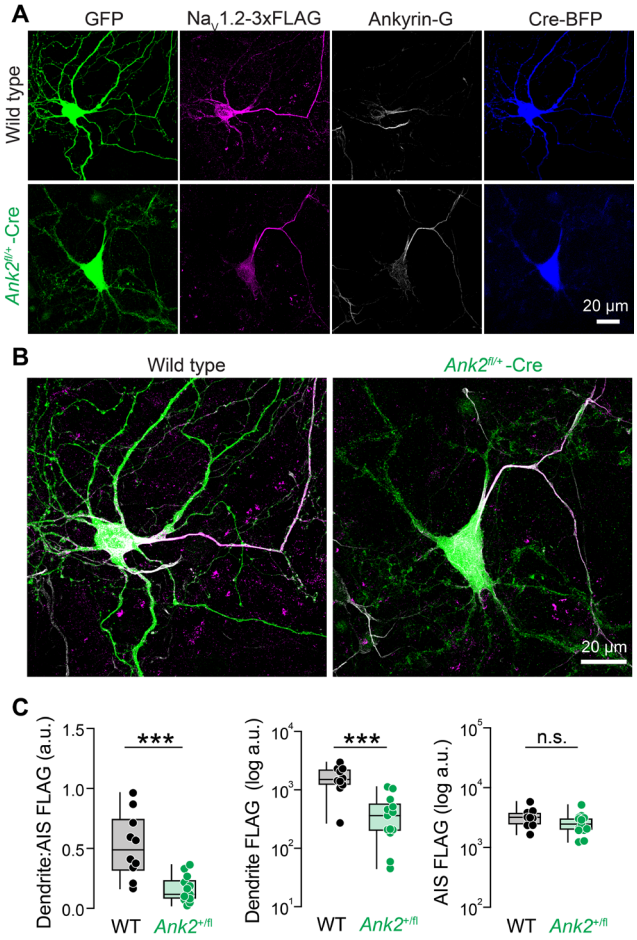

Figure S4: Loss of Nav1.2 localization to the dendritic membrane of cultured *Ank2* heterozygous neurons. Related to Figs. 2-3.

(A) Confocal images of DIV21 neocortical *Ank2*$^{+/fl}$ neurons transfected with Nav1.2-3xFLAG-IRES-eGFP and either BFP (WT) or Cre-2A-BFP (*Ank2* heterozygous). Cells were immunostained with antibodies against endogenous ankyrin-G (white), FLAG (magenta), GFP (green), and BFP (blue). Top right: zoomed images of dendrite labeled with yellow box.

(B) Merged images from (A) with the exclusion of BFP.

(C) Quantification of mean fluorescence intensity of Nav1.2-3xFLAG in dendrites relative to AIS. Circles represent individual neurons. (WT: 0.52 ± 0.09, n = 10 cells; *Ank*$^{+/fl}$: 0.16 ± 0.03, n = 13 cells). ***p = 0.0002. Mann-Whitney test. Mean fluorescence intensity of Nav1.2-3xFLAG in dendrites. (WT: 1659 ± 241.8, n = 10 cells; *Ank*$^{+/fl}$: 425.3 ± 96.09, n = 13 cells). ***p = 0.0001. Mann-Whitney test. Mean fluorescence intensity of Nav1.2-3xFLAG in the AIS. (WT: 3336 ± 365.7, n = 10 cells; *Ank*$^{+/fl:}$ 2593 ± 288.4, n = 13 cells). p = 0.09. Mann-Whitney test.

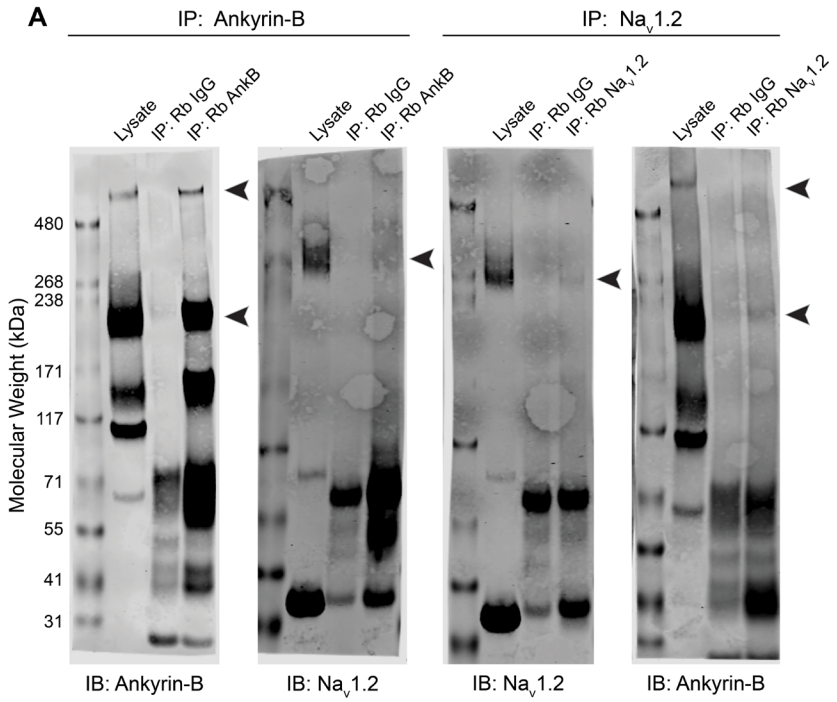

Figure S5: Co-Immunoprecipitation of endogenous ankyrin-B and Na$_V$1.2 from adult mouse brain. Related to Fig. 3.

(A) Full membranes of Co-IP western blots from Figure 3E. Left: IP of endogenous ankyrin-B and western blot of IP lysates probed with antibodies to ankyrin-B or endogenous Na$_V$1.2 from P60-P75 mice. Right: IP of endogenous Na$_V$1.2 and western blot of IP lysates probed with antibodies to Na$_V$1.2 or ankyrin-B from P60-P75 mice. Black arrows highlight bands of ankyrin-B or Na$_V$1.2. Non-immune IgG used as a negative control.

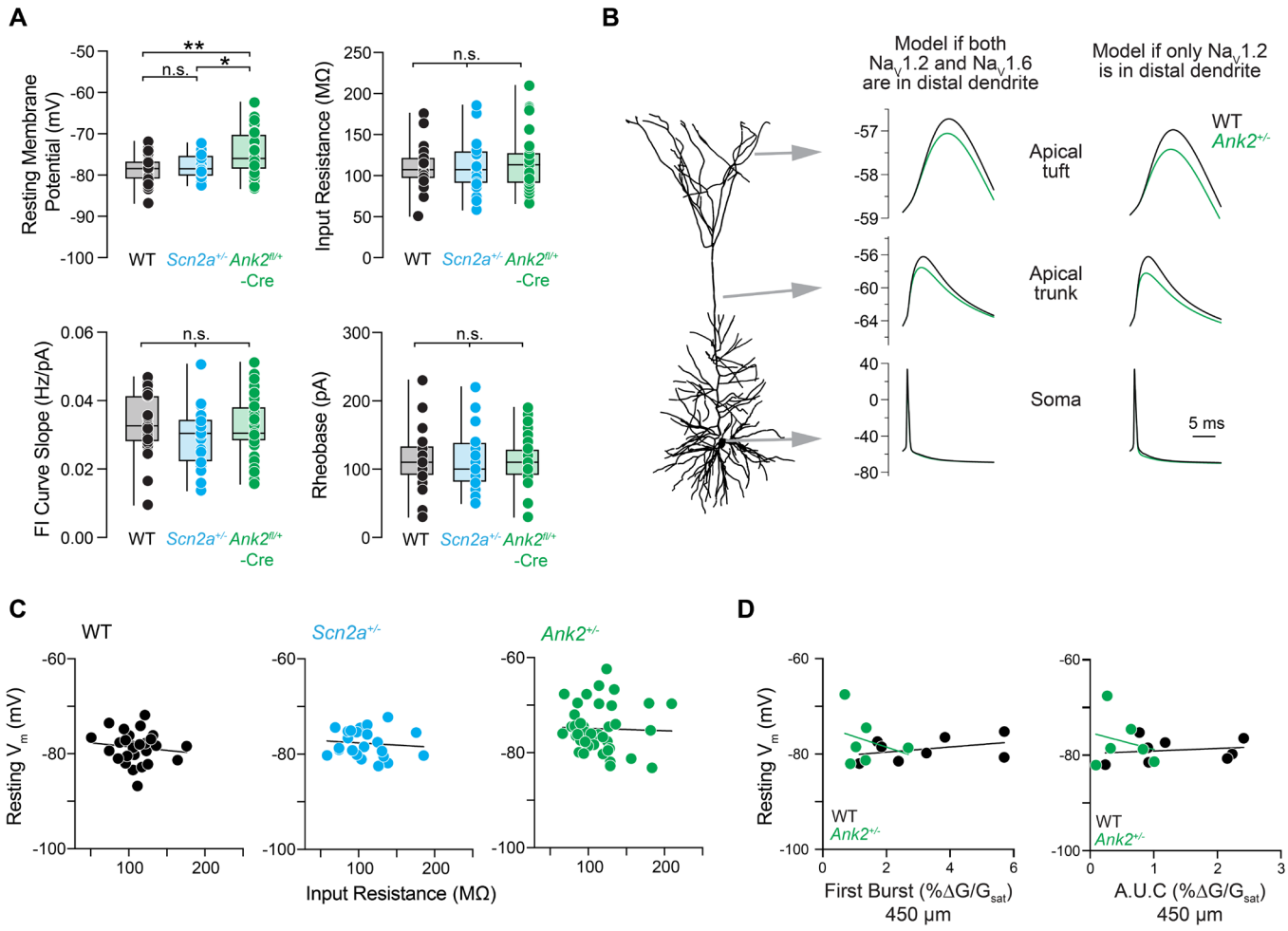

Figure S6: Additional modeling and intrinsic electrophysiological measurements from conditional *Ank2*$^{+/fl}$-Cre mice. Related to Fig. 4.

(A) Empirical electrophysiological recordings from P43-75 WT (black), *Scn2a*$^{+/-}$ (cyan) vs. *Ank2*$^{+/fl}$-Cre (green) L5 thick-tufted pyramidal neurons. Circles represent single cells. Resting membrane potential (mV) – (WT: -78.7 ± 0.6 mV, n = 27 cells, N = 14 mice; *Scn2a*$^{+/-}$: -77.7 ± 0.6 mV, n = 23 cells, N = 8 mice; *Ank2*$^{+/fl}$-Cre: -74.9 ± 0.8 mV, n = 39 cells. N = 16 mice). WT vs. *Scn2a*$^{+/-}$ p = 0.7, WT vs *Ank2*$^{+/fl}$-Cre **p = 0.001, *Scn2a*$^{+/-}$ vs. *Ank2*$^{+/fl}$-Cre *p = 0.03. Holm-Šídák multiple comparisons test. Input resistance (MΩ) – (WT: 109.9 ± 5.0 MΩ, n = 27 cells; *Scn2a*$^{+/-}$: 109.9 ± 5.7 MΩ, n = 27 cells; *Ank2*$^{+/fl}$-Cre: 114.5 ± 5.3 MΩ, n = 39 cells). No significant differences. Holm-Šídák multiple comparisons test. FI curve slope (Hz/pA) - (WT: 0.033 ± 0.002 Hz/pA, n = 29 cells; *Scn2a*$^{+/-}$: 0.03 ± 0.002 Hz/pA, n = 23 cells, *Ank2*$^{+/fl}$-Cre: 0.033 ± 0.001, n = 39 cells). No significant differences. Holm-Šídák multiple comparisons test. Rheobase rheobase current (pA) to generate first spike – (WT: 116.6 ± 7.9 pA, n = 29 cells; *Scn2a*$^{+/-}$: 115.2 ± 10.0 pA, n = 23 cells; *Ank2*$^{+/fl}$-Cre: 112.1 ± 5.6 pA, n = 39 cells). No significant differences. Holm-Šídák multiple comparisons test.

(B) Compartmental modeling of the effects of *Ank2* haploinsufficiency, and presumed resultant 50% reduction in Nav1.2 density in regions of dendrite >30 µm from the soma. Two models are considered: a model similar to that in Spratt et al., 2019 where both Nav1.2 and Nav1.6 are expressed in equal densities in dendrites (left), and a revised model in which Nav1.2 is the only sodium channel proteoforms expressed in distal dendrites. In both cases, *Ank2*$^{+/-}$ conditions are modeled as a 50% reduction in Nav1.2 density within more distal dendritic compartments only (e.g., soma and proximal dendrites maintain WT levels of Nav1.2).

(C) Correlation of resting membrane potential (V_m) versus input resistance in WT (black), *Scn2a*$^{+/-}$ (cyan), and *Ank2*$^{+/fl}$-Cre (green) L5 pyramidal neurons. Simple linear regression – (WT: R-squared = 0.02, p = 0.5, not significant; *Scn2a*$^{+/-}$: R-squared = 0.01, p = 0.6, not significant; *Ank2*$^{+/fl}$-Cre: R-squared = 0.001, p = 0.8, not significant).

(D) Correlation between resting membrane potential (V_m) versus AP backpropagation first burst amplitude (left) and area under the curve (A.U.C.) (right) at 450 µm from soma in apical dendrites of WT (black) and *Ank2*$^{+/fl}$-Cre (green) neurons. First Burst Amplitude simple linear regression – (WT: R-squared = 0.15, p = 0.3, not significant; *Ank2*$^{+/fl}$-Cre: R-squared = 0.09, p = 0.4, not significant). AUC simple linear regression – (WT: R-squared = 0.03, p = 0.7, not significant; *Ank2*$^{+/fl}$-Cre: R-squared = 0.05, p = 0.7, not significant).

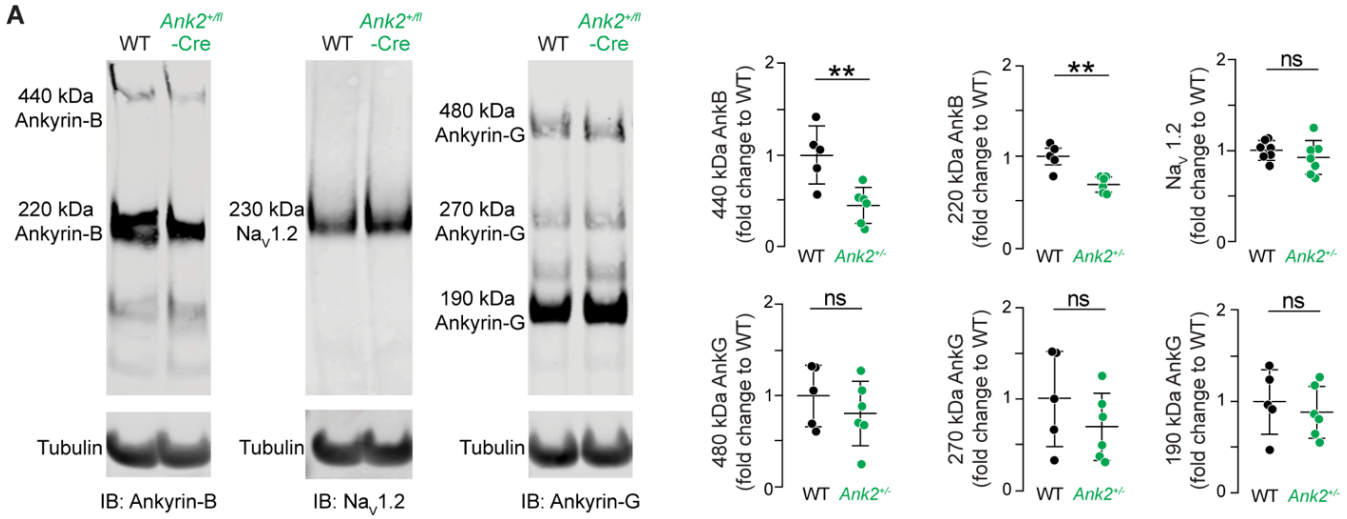

Figure S7: Western blot of ankyrins and Na$_V$1.2 from *Ank2*$^{+/fl}$::CaMKIIα-Cre adult mouse brain. Related to Figs. 5-7.

(A) Western blot of neocortical lysates of P60 WT (black) and *Ank2*$^{+/fl}$::CaMKIIα-Cre (green) mice. Left: Western blots probed with anti-total ankyrin-B and anti-α-tubulin. 440 kDa ankyrin-B – WT: 1.0 ± 0.14, N = 5 mice; *Ank2*$^{+/fl}$-Cre: 0.45 ± 0.1, N = 6 mice) **p = 0.009. Mann-Whitney test. 220 kDa ankyrin-B – (WT: 1.0 ± 0.06, N = 5 mice; *Ank2*$^{+/fl}$-Cre: 0.7 ± 0.03, N = 6 mice) **p = 0.004. Mann-Whitney test. Middle: Probed with anti-Na$_V$1.2 and anti-tubulin. Na$_V$1.2 – (WT: 1.0 ± 0.04, N = 7 mice; *Ank2*$^{+/fl}$-Cre: 0.93 ± 0.08, N = 7 mice) p = 0.32. Mann-Whitney test. Right: probed with anti-total ankyrin-G and anti-tubulin. 480 kDa ankyrin-G – (WT: 1.0 ± 0.15, N = 5 mice; *Ank2*$^{+/fl}$-Cre: 0.81 ± 0.1, N = 6 mice) p = 0.54. Mann-Whitney test. 270 kDa ankyrin-G – (WT: 1.0 ± 0.2, N = 5 mice; *Ank2*$^{+/fl}$-Cre: 0.7 ± 0.2, N = 6 mice) p = 0.33. Mann-Whitney test. 190 kDa ankyrin-G – (WT: 1.0 ± 0.2, N = 5 mice; *Ank2*$^{+/fl}$-Cre: 0.88 ± 0.1, N = 6 mice) p = 0.54. Mann-Whitney test.

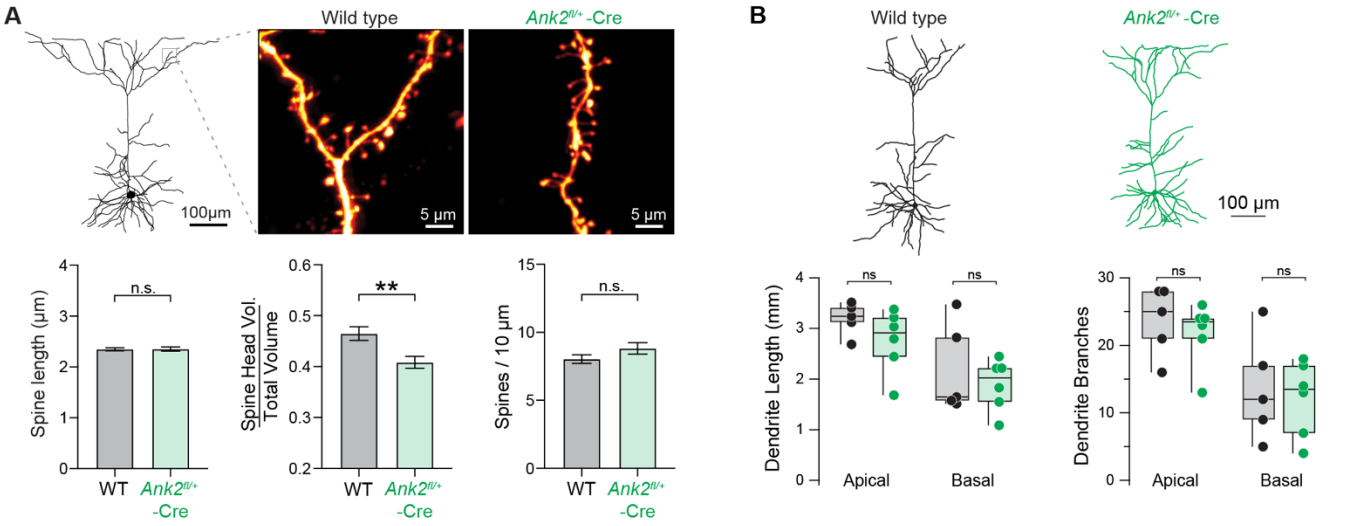

Figure S8: Dendritic spines are morphologically immature in *Ank2*$^{+/fl}$-Cre neurons. Related to Figs. 5-7.

(A) Top: Examples of spines along apical tuft dendritic branches of P42-65 WT (black) and *Ank2*$^{+/fl}$::CaMKIIα-Cre mice (green). Bottom: Spine length – (WT: 2.4 µm ± 0.03, n = 1044 spines; *Ank2*$^{+/fl}$-Cre: 2.4 ± 0.4 µm, n = 787 spines) p = 0.96. Mixed-effects analysis. Spine head volume/total volume – (WT: 0.47 ± 0.01, n = 1044 spines; *Ank2*$^{+/fl}$-Cre: 0.41 ± 0.01 , n = 782 spines) **p = 0.0087. Mixed-effects analysis. Spines/10 µm– (WT: 8.04 ± 0.32, n = 36 branches; *Ank2*$^{+/fl}$-Cre: 8.82 ± 0.43, n = 28 branches) p = 0.12. Mann-Whitney test.

(B) Top: Representative tracings of L5 thick-tufted neurons from P52-67 WT (black) and *Ank2*$^{+/fl}$::CaMKIIα-Cre mice (green) mice generated from 2PLSM z-stacks of Alexa 594-filled neurons. Left: Dendritic length (mm) of apical and basal dendrites. Apical – (WT: 3.2 ± 0.1 mm, n = 5 cells; *Ank2*$^{+/fl}$-Cre: 2.8 ± 2.5 mm, n = 6 cells). p = 0.18. Mann-Whitney test. Basal – (WT: 2.2 ± 0.4 mm, n = 5 cells; *Ank2*$^{+/fl}$-Cre: 1.9 ± 0.2 mm, n = 6 cells). p = 0.8. Mann-Whitney test. Right: Overall number of branch points per cell. Apical – (WT: 23.6 ± 2.3, n = 5 cells; *Ank2*$^{+/fl}$-Cre: 21.8 ± 1.9, n = 6 cells). p = 0.46. Mann-Whitney test. Basal – (WT: 13.6 ± 3.5, n = 5 cells; *Ank2*$^{+/fl}$-Cre: 12.17 ± 2.3, n = 6 cells). p = 0.97. Mann-Whitney test.

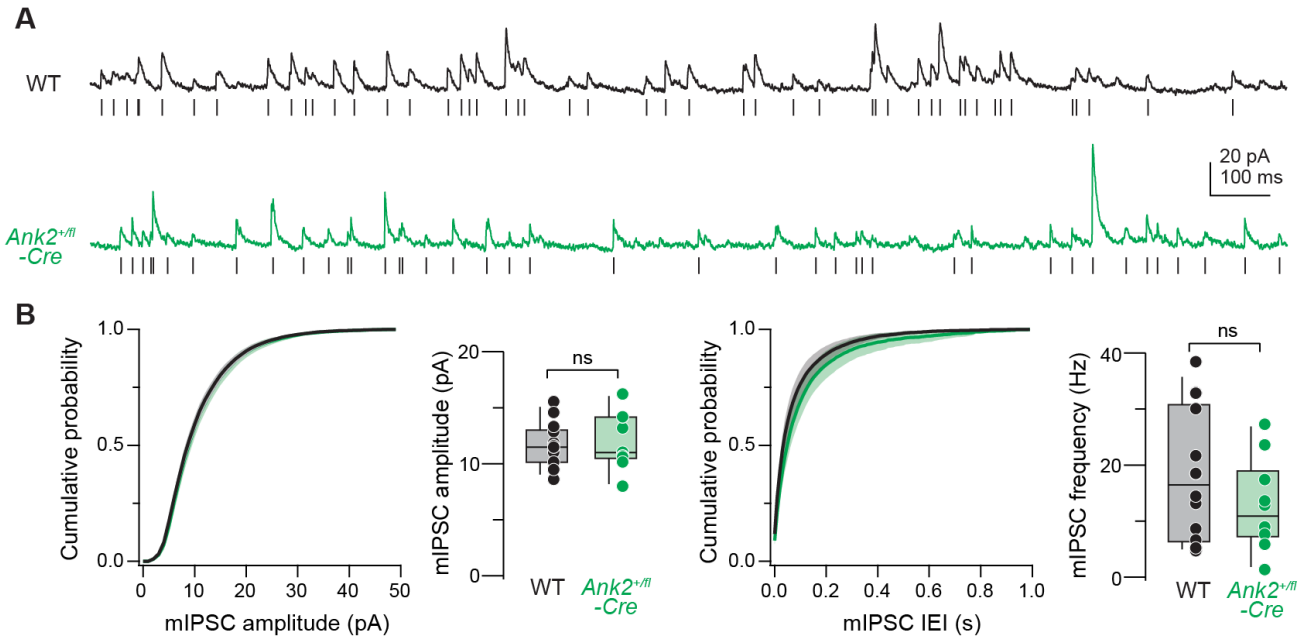

Figure S9: Miniature inhibitory postsynaptic currents from *Ank2*$^{+/fl}$-Cre L5 pyramidal neurons. Related to Fig. 6.

(A) mIPSCs recorded from P54-P60 WT (black) and *Ank2*$^{+/fl}$-Cre-mCherry-positive (green) L5 pyramidal neurons at 0 mV. Ticks denote detected events. Cumulative probability histograms were generated per cell and then averaged. Circles represent individual neurons. Left: Cumulative probability distribution and mIPSC amplitude (pA) – (WT: 11.7 ± 0.5 pA, n = 14 cells; *Ank2*$^{+/fl}$-Cre: 11.9 ± 0.8 pA, n = 10 cells). p > 0.99. Mann-Whitney test. Right: Cumulative probability distribution of mIPSC inter-event intervals (IEI) and average frequency (Hz) – (WT: 17.9 ± 3.1 Hz, n = 14 cells; *Ank2*$^{+/fl}$-Cre: 12.8 ± 2.5 Hz, n = 10 cells). p = 0.4. Mann-Whitney test.

Supplemental Table 1: Conductance values for $Na_V1.2$ and $Na_V1.6$ in WT conditions in all compartments, Related to Figure 4.

Compartment	**Conductance (mho/cm^2)**	**Model with both $Na_V1.2$ and $Na_V1.6$ in distal dendrite**	**Model with $Na_V1.2$ alone in distal dendrite**
Soma	$Na_V1.2$	0.04840837	0.04840837
	$Na_V1.6$	0.04840837	0.04840837
Proximal AIS (peak)	$Na_V1.2$	20	20
	$Na_V1.6$	28	28
Distal AIS (peak)	$Na_V1.2$	0	0
	$Na_V1.6$	28	28
Axon	$Na_V1.2$	0	0
	$Na_V1.6$	0.0983955	0.0983955
Axon nodes	$Na_V1.2$	0	0
	$Na_V1.6$	2	2
Proximal dendrite	$Na_V1.2$	2.2877E-07	2.2877E-07
	$Na_V1.6$	2.2877E-07	2.2877E-07
Distal dendrite	$Na_V1.2$	2.2877E-07	8.6932E-07
	$Na_V1.6$	2.2877E-07	0